Quantum Quenching in Two-Dimensional Spin-1 Bose Gases

S. D. CHEN

SUPERVISOR: DR. P. B. BLAKIE

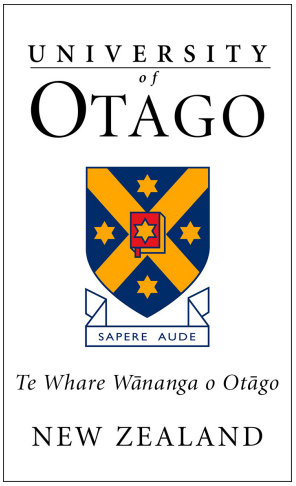

A dissertation submitted in partial fulfillment for
the degree of Bachelor of Science with Honours in Physics

September 2013

Abstract

Structure formation in spinor Bose-Einstein condensate are systems of significant interest: they have both superfluid and magnetic order, lending themselves interesting dynamical textures after a quench. Following previous theoretical work on quenches from finite to zero magnetic field, we explore the consequences of quenching to a variety of different final magnetic field strengths in this dissertation — not just zero. Our studies begin with developing an algorithm to propagate this complex, multi-modal system using an adaptive-step Runge-Kutta-based partial differential equation solver. We use this to evolve trajectories that approximately describe the full quantum field dynamics using the Truncated Wigner formalism. In our results we observe a quenched spinor condensate reorganize itself for various different quench depths, observing experimentally-known phenomenon such as spontaneous magnetization, coarsening in long-time dynamics, and domain formation. We also observe never-before seen behavior, including the light-cone-esque propagation of correlations in the shallow quench regime, and a gradual spontaneous ordering of the mean correlation

Acknowledgments

Thanks first and foremost to Blair, my supervisor, without whom I would be a lost mess in the intimidating and confusing world of Real Science. Thanks for putting up with me, and my endless laments of "but what does it *mean?*". Blair has a knack for explaining complex concepts in an accessible way, and has many unique insights which have been invaluable.

Thanks also to Ashton, for answering the odd question when Blair was away. To Danny, for helping set up Thunderbirds. Thanks to Luke and Edward for useful discussions.

To everyone in the honours room — you're all awesome. Thanks for putting up with my terribad jokes. For making thesis season bearable. I wish you all the best for the future; I know you're all be amazing at whatever you might do.

To Tom, thanks for looking after me when I would often forget to look after myself. Thanks for putting up with the late nights (and sometimes no-nights!).

And of course, to my parents. For all you've sacrificed to give your daughters a good life; for giving me unconditional support in all the crazy projects I decide to take up. Take care of yourselves.

Abbreviation	Definition
BEC	Bose-Einstein Condensate
GPE	Gross-Pitaevskii Equation
PGPE	Projected Gross-Pitaevskii Equation
SMA	Single Mode Approximation
SO(3)	Special Orthogonal Group of all 3D rotations
SU(2)	Special Unitary Group (spin space)
U(1)	Unitary Group
VKRF45	Vectorized Runge-Kutta-Felhberg to 4th and 5th order

Contents

Chapter 1

Introduction

A lecturer in second year once told our class that the goal of physics was to predict the future. This is child's play for linear, well-behaved systems away from the deathly touch of chaos, but for most systems — especially those transitioning between phases — this is not so trivial. Symmetry breaking phase transitions are a fundamental physical process that appears in scenarios ranging from superfluid helium[1] to the early dynamics of the universe[2]. In this thesis we look at the equilibriation dynamics of spinor Bose-Einstein condensates (BECs).

First theorized by S. N. Bose in 1924[3] and experimentally realized in 1995[4], Bose-Einstein condensation is a highly coherent state of matter that provides us with an extremely unique opportunity. BECs have highly tunable interactions that we can control using Feshbach resonances[5]. In addition, they equilibriate slowly — spinor condensates slower still[6]. These systems give us a unique chance to perform a quantum quench and actually watch the system *reorganize itself*.

When we "quench" a system, we change its parameters on a timescale much shorter than its healing time — much like a blacksmith dipping a hot sword into cold water. In a quantum spinor system it's a magnetic field, instead of temperature, that we dial back. This translates to exponentially growing excitations that manifest themselves as magnetic domains. This structure comes about from the spontaneously broken symmetry by quantum fluctuations during a quench through a multicritical point; a phase transition.

Previous work on quenched spinor condensates[7] has found that some dynamics are reasonably well described by a linearized theory (which we introduce in the next chapter). In 2011, in an investigation into thermalization dynamics, Barnett *et al.* concluded that the quenched system does not thermalize at all[8]. Instead it reaches a quasisteady ("prethermalized") phase, with domains that grow randomly over time. Interestingly enough, such prethermalized regimes also turn up in atomic superfluids[9].

In this work we explore the results seen by Barnett *et al.* for a two-dimensional spin-1 condensate. Simulation code is developed from the ground up, tested by reproducing experimentally known phenomena, and finally used to investigate quenching dynamics. We make use of the spinor Gross-Pitaevskii equations, and Bogoliubov theory to analytically explore instabilities around a quench.

Our goals for this research are to *a*) develop working code that accurately simulates an interacting spin-1 Bose system; *b*) reproduce the results of Barnett *et al.*'s 2011 paper; *c*) investigate the effect on domain formation of different quench depths; and *d*) determine the boundaries of different quench regimes, if any.

In chapter 2, we outline the background theory needed to begin our investigation. Included is an overview of the different ground state phases and spin dynamics in a spinor condensate, so that we may develop an initial intuition for these highly quantum systems. Chapter 3 discusses the numerical essentials of our project — how we developed our code and the tests to justify it. Finally, chapter 4 goes through the simulation results.

Chapter 2

Preliminaries

Quantum systems are notorious for being counterintuitive; strange and hostile. In this chapter we go through some fundamental concepts of Bose-Einstein condensation, moving onto spinor condensates and the mean-field theory so often used to describe them. After building some rapport with our system, we discuss Bogoliubov theory; its formalism, excitation spectra, and we derive the spinor Gross-Pitaevskii equations along the way. We then move on to learn about all the interesting dynamics a spinor BEC has to offer — its different phases, spin-mixing, and, of course, quenching dynamics.

2.1 The Spinor Condensate

Bose-Einstein condensation is an impressive demonstration of the peculiar concept of *wave-particle duality*, where at low energies particles become waves are start superimposing on its neighbors. It's characterized by a macroscopic occupation of the lowest energy mode, where all atoms collapse to the same quantum state. Cooling a Bose gas past a critical temperature (often only a few hundred nanokelvin above absolute zero) initiates this phase transition. A pure Bose-Einstein condensate at $T = 0$ can be thought of as a gas of atoms undergoing an identity crisis — every single atom, remarkably, has the same wavefunction:

$$\varphi_0 = |\varphi_0| e^{i\theta}, \tag{2.1}$$

This acts as an *order parameter*, and dictates most properties of the system. Scalar condensates are said to have $U(1)$ gauge symmetry; i.e., it has a free "choice" of phase θ in Eq. (2.1) without affecting any physical properties of the state.

2.1.1 Spin Degrees of Freedom

Atoms making up our Bose gas typically have a number of spin states. At low magnetic fields, these states become accessible, allowing the condensate to have *spin* degrees of freedom. This condensate is known as a spinor BEC.

At low magnetic fields, the Zeeman effect fades (See Fig. 2.1) and the hyperfine interaction between the spin states of an atom dominates. Instead of there being one lowest ground state, a three-way degeneracy is

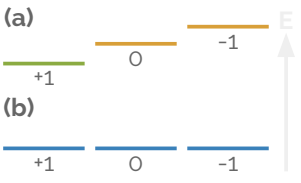

Figure 2.1: Hyperfine energy levels of the $F = 1$ atom (a) with the Zeeman effect, where an external magnetic field shifts the energy levels. In (b) the field is turned off, and all three hyperfine states become degenerate.

born — the condensate can now "choose" a spin state. In a spin system, the symmetry can be broken in many ways; leading to more flavorful interactions such as spin currents[10], dipolar gases[11], and spontaneous magnetization[12]. Now we have something new — instead of a scalar order parameter, our condensate is now described by a complex *vector* order parameter:

$$\Psi_0 = \sqrt{n_0}\begin{pmatrix}\psi_+\\ \psi_0\\ \psi_-\end{pmatrix} \tag{2.2}$$

where n_0 is the number density and ψ_m are the $+1, 0, -1$ components[1].

[1] In this thesis we consider only spin-1 atoms.

A non-zero spin gives the atom a small magnetic moment — our system can now display novel phenomena such as magnetization textures. Taking the spin-1 vector, $\mathbf{f} = (f_x, f_y, f_z)^{\mathrm{T}}$ with components:

$$f_x = \frac{\hbar}{\sqrt{2}}\begin{pmatrix}0&1&0\\1&0&1\\0&1&0\end{pmatrix}, \qquad f_y = \frac{\hbar}{\sqrt{2}}\begin{pmatrix}0&-i&0\\i&0&-i\\0&i&0\end{pmatrix}, \qquad f_z = \hbar\begin{pmatrix}1&0&0\\0&0&0\\0&0&-1\end{pmatrix}$$

(which are simply rotation matrices in spin ($SU(2)$) space), we can compute expressions for longitudinal (pointing out of the plane),

$$\begin{aligned} F_z &= \Psi_0^\dagger f_z \Psi_0 \\ &= n_0\left(|\psi_+|^2 - |\psi_-|^2\right) \end{aligned} \tag{2.3}$$

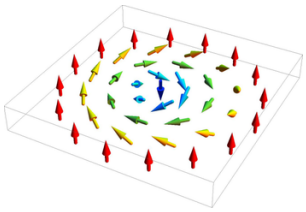

Figure 2.2: Interesting new magnetization effects include the formation of spin (skyrmion) vortices.

and transverse (pointing around inside the plane) magnetizations

$$\begin{aligned} F_x &= \Psi_0^\dagger f_x \Psi_0 \\ &= \frac{n_0}{\sqrt{2}}\left(\psi_+^\dagger\psi_0 + \psi_0^\dagger\psi_- + \psi_+\psi_0^\dagger + \psi_0\psi_-^\dagger\right) \end{aligned} \tag{2.4}$$

$$\begin{aligned} F_y &= \Psi_0^\dagger f_y \Psi_0 \\ &= \frac{1}{\sqrt{2}}\left(\psi_+^\dagger\psi_0 + \psi_0^\dagger\psi_- - \psi_+\psi_0^\dagger - \psi_0\psi_-^\dagger\right) \end{aligned} \tag{2.5}$$

where F_x and F_y are sometimes given in terms of F_+ and F_-:

$$F_+ = F_x + iF_y \tag{2.6a}$$

$$F_- = F_x - iF_y \tag{2.6b}$$

With these we construct the spin-density vector, $\mathbf{F} = (F_x, F_y, F_z)^{\mathrm{T}}$.

Unsurprisingly, spinor condensates are highly susceptible to magnetic fields, allowing the experimentalist to create new ground-state phases by varying an external magnetic field (see Sec. 2.1.4).

2.1.2 The Spinor Hamiltonian

Our system's Hamiltonian is given by[13]:

$$\mathcal{H} = \mathcal{H}_0 + \mathcal{H}_{int} \tag{2.7}$$

where

$$\mathcal{H}_0 = \int dr \Psi^\dagger\left(-\frac{\hbar^2}{2m}\nabla^2 + V_{ext}(r) + qf_z^2\right)\Psi \quad , \quad \text{and} \tag{2.8}$$

$$\mathcal{H}_{int} = \int dr \frac{1}{2}g_n n_0^2 + \frac{1}{2}g_s\langle\mathbf{f}\rangle^2 \tag{2.9}$$

The first term (2.8) is known as the free Hamiltonian, where $V_{ext}(r)$ is the external trapping potential and $q \sim B^2$ is the quadratic Zeeman shift. In the interaction Hamiltonian (2.9), $\langle \mathbf{f} \rangle \equiv \psi_a^* \mathbf{f}_{ab} \psi_b$.

Note that there is an implied summation over the repeated indicies a and b. They are summed over the three spin states; $-1, 0$ and 1.

Amazingly, all particle and spin interactions are expressed with just two parameters; g_n and g_s, respectively. This is thanks to the low energy of atoms in the condensate which allow us to approximate the interaction potentials by simple contact interactions:

$$\lim_{k \to 0} V(r) = g\delta(r) \tag{2.10}$$

The particle and spin interaction parameters can thus be given in just the terms of the s-wave scattering lengths:

$$g_n = \frac{4\pi\hbar^2}{3m}(a_0 + 2a_2), \quad \text{and} \quad g_s = \frac{4\pi\hbar^2}{3m}(a_2 - a_0) \tag{2.11}$$

where a_0 and a_2 are the scattering lengths for the particle and spin interactions, respectively.

In a spinor BEC, the two interaction parameters have the following physical meanings:

$g_n > 0$	repulsive density interaction
$g_n < 0$	attractive particle-particle interaction (unstable)
$g_s > 0$	antiferromagnetic spin interactions
$g_s < 0$	ferromagnetic spin interactions

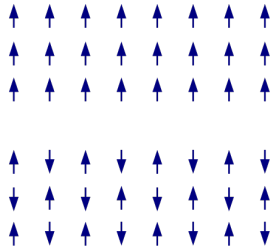

Figure 2.3: Ferromagnetic and antiferromagnetic orderings (the vertical axis is the z axis).

Note that in any case we will need to have a positive g_n for our condensate to be mechanically stable, else the entire system collapses. An antiferromagnetic system means that it favors minimizing the $\langle \mathbf{f} \rangle^2$ in (2.9), while a ferromagnetic system wants to *maximize* $\langle \mathbf{f} \rangle^2$.

For this thesis we focus on the spin dynamics of ^{87}Rb, which has a repulsive particle-particle interaction and a ferromagnetic spin interaction, so that excluding the influence of an external magnetic field, the system likes to locally magnetize.

2.1.3 Gross-Pitaevskii Equations

From Hamiltonian given in Eq. (2.7), and dropping the zero subscripts on our order parameter, one can obtain the energy functional for the system:

$$E(\Psi^*, \Psi) = \int \left[\frac{\hbar^2}{2m} |\nabla \Psi|^2 + V_{ext}(r)|\Psi|^2 + \frac{1}{2} g_n |\Psi|^4 + \frac{1}{2} g_s |\Psi^* \mathbf{f} \Psi|^2 \right] dr \tag{2.12}$$

which we will minimize to determine the spinor ground states. Such ground states satisfy the so-called time-independent Gross-Pitaevskii equations:

$$\mu \psi_m = \frac{\partial}{\partial \psi_m^*} E(\Psi^*, \Psi) \quad , \quad m = +1, 0, -1 \tag{2.13}$$

where $\mu = g_n n_0$ is the chemical potential. This describes the system at its steady equilibrium. More generally, the spinor condensate evolves dynamically according to:[2]

$$i\hbar \frac{\partial \psi_m}{\partial t} = \frac{\partial}{\partial \psi_m^*} E(\Psi^*, \Psi) \quad , \quad m = +1, 0, -1 \tag{2.14}$$

[2] This comes from the Heisenberg equation of motion for a diagonalized Hamiltonian using Bogoliubov transformations. A full derivation of these equations can be found in Ref.[14]

Explicitly writing out each component of Eq. (2.14), we get the three coupled spinor Gross-Pitaevskii equations:

$$i\hbar\frac{\partial\psi_+}{\partial t} = \left[-\frac{\hbar^2}{2m}\nabla^2 - p + q + g_n|\Psi|^2 + g_s(|\psi_+|^2 + |\psi_0|^2 - |\psi_-|^2)\right]\psi_+ + g_s\psi_-^*\psi_0^2 \tag{2.15a}$$

$$i\hbar\frac{\partial\psi_0}{\partial t} = \left[-\frac{\hbar^2}{2m}\nabla^2 + g_n|\Psi|^2 + g_s(|\psi_+|^2 + |\psi_-|^2)\right]\psi_0 + 2g_s\psi_+\psi_0^*\psi_- \tag{2.15b}$$

$$i\hbar\frac{\partial\psi_-}{\partial t} = \left[-\frac{\hbar^2}{2m}\nabla^2 + p + q + g_n|\Psi|^2 + g_s(|\psi_-|^2 + |\psi_0|^2 - |\psi_+|^2)\right]\psi_- + g_s\psi_+^*\psi_0^2 \tag{2.15c}$$

By solving the steady-state equations (2.13), we can look at the ground-state phases and excitation spectra. The dynamical GPEs (2.15) will be used to propagate a simulated system in time.

2.1.4 Phases of a Spin-1 Condensate

Seminal studies by Stenger *et al.*[15] showed clear spin phases depending on the variation of an external magnetic field, given by the linear (p) and quadratic (q) Zeeman parameters.

The ground state wavefunction is found by minimizing the energy functional in Eq. (2.12) in the *Thomas-Fermi approximation*, where kinetic energy terms are neglected. Looking at the ferromagnetic case for ^{87}Rb (Fig. 2.4(c)), we find that the linear Zeeman field corresponds to the overall magnetization of our condensate, lifting or lowering the spinors out of the plane, giving preference to the $m = \pm 1$ states, and hence a non-zero F_z.

This gives the ferromagnetic phases for $q \leq 0$ and $p \neq 0$, located to the left of the red lines in Fig. 2.4.

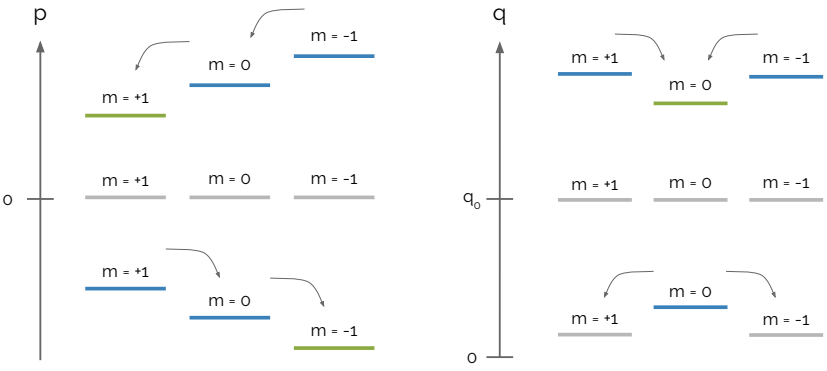

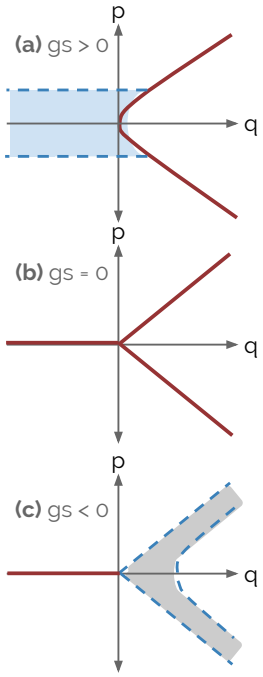

Figure 2.4: Phase diagrams for (a) $g_s > 0$, (b) $g_s = 0$, and (c) $g_s < 0$. The blue and gray shaded regions indicate antiferromagnetic and broken-axis phases, respectively.

Figure 2.5: The effect of linear and quadratic Zeemans on the $F = 1$ hyperfine levels.

The quadratic Zeeman effect is more subtle; it favors the $m = 0$ state for $q > 0$, and the $m = \pm 1$ states for $q < 0$. For high q values, this translates into a polar ($\Psi = (0, 1, 0)^{\mathrm{T}}$) ground state.

In the shaded region of Fig. 2.6, between $p = q$ and $p^2 = q^2 - q \times 2|g_s|n_0$, there exists the so-called *broken axis* phase, where spinors with non-zero F_x and F_y components are lifted out of the plane. In this region one may picture a tug-of-war between the quadratic Zeeman (which prefers the $m = 0$ state) and the interaction energies (which favor the $m = \pm 1$ states)[3].

[3] This tug-of-war is what causes spin mixing dynamics, which we will talk about in the next section.

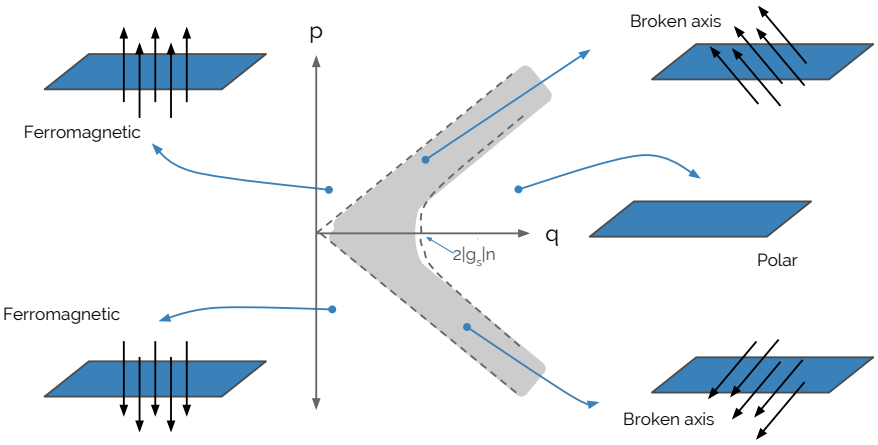

Figure 2.6: Schematic diagram for the different phases for the ferromagnetic case, such as 87Rb.

Additionally, we note that the broken-axis region has a second order phase boundary — the transition is gradual and the phase domains miscible.

Note that the $|0\rangle \rightarrow |+1\rangle$ OR $|-1\rangle$ population exchange shown in the bottom-right-hand corner of Fig. 2.5 is a symmetry-breaking process and thus the transition from the polar to broken-axis phase is a symmetry-breaking phase transition.

2.1.5 Spontaneous Symmetry Breaking

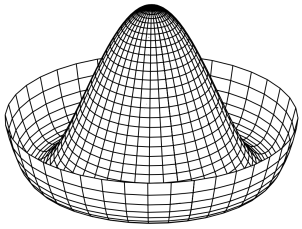

Figure 2.7: Goldstone's Mexican hat potential, exhibiting $U(1)$ gauge symmetry. At the peak the system symmetric, but once it falls to a stable low-energy state it breaks said symmetry.

In a spinor Bose-Einstein condensate, there exists both gauge symmetry (free choice of phase), and spin symmetry (free choice of spin state). The ground states are degenerate and lie symmetrically around our system — there is no one single favored state.

Below a critical temperature, the atoms Bose condense into a single state. To us, the outside observers, the system appears to have arbitrarily "chosen" a single state out of many equally favorable ones. In the act of equilibriating to this new phase of matter, the system has spontaneously broken the symmetry.

Symmetry breaking is the physicist's version of a hurricane after the proverbial butterfly flaps its wings. When a system crosses a critical point, it is the small quantum fluctuations that determine which branch of a bifurcation is taken, and hence the system's ultimate fate.

Symmetries of a system also relate closely to conservation laws[4]. Here the $U(1)$ symmetry corresponds to a conservation of particle number, while the $SU(2)$ corresponds to a conservation of total magnetization.

[4] If the reader is interested, one may want to look up the Ward-Takahashi identity; or, for a classical (and more accessible) analog, check out Noether's theorem.

When a system spontaneously breaks a continuous symmetry, Nambu-Goldstone modes necessarily appear[16, 17]. These are long-wavelength, spinless excitations, generated for each broken symmetry that does not preserve the ground state[18].

Here is a nice segway for us to discuss the *Bogoliubov* excitation spectrum, which is a special case of Nambu-Goldstone modes for weakly-interacting Bose gases.

2.2 Bogoliubov Theory

In the mean-field theory, one argues that in the dilute, low-energy limit of $T \approx 0$, we can effectively ignore quantum and thermal fluctuations and replace the field operator (which describes our condensate) with its expectation value[5]:

$$\hat{\Psi} = \langle \hat{\Psi} \rangle \equiv \Psi_0 \qquad , \qquad \langle \hat{\Psi}^\dagger \hat{\Psi} \rangle = |\Psi_0|^2 = n_0 \tag{2.16}$$

[5] One must be careful about doing this, as it breaks $U(1)$ symmetry and hence number conservation. As long as we fulfill orthonormality and completeness conditions in our expansion of the field operator, we should be fine.

Here, we assume equilibrium, and Ψ is the three-component, spinor order parameter as described in the previous section. This is all good and well for simplifying calculations, but not very interesting if we want to consider at least *some* fluctuations.

Bogoliubov theory is a perturbative theory[19] that expands small quantum fluctuations around the mean-field ground state Ψ_0 up to quadratic order. We now consider the fluctuations of the field operator:

$$\hat{\Psi} = \Psi_0 + \delta\hat{\Psi} \tag{2.17}$$

where the fluctuation term satisfies $\langle \delta\hat{\Psi} \rangle = 0$. This is known as the *Bogoliubov ansatz*.

2.2.1 The Uniform Condensate

In this thesis we consider a uniform condensate ($V_{ext} = 0$) in a box of volume L^3, which is an infinite uniform condensate with periodic boundary conditions at the edges of the box. These boundary conditions give us a plane-wave expansion of the field operator:

$$\hat{\psi}_m = \frac{1}{\sqrt{L^3}} \sum_{\mathbf{k}} \hat{a}_{\mathbf{k},m} e^{i\mathbf{k}\cdot\mathbf{r}} \qquad , \qquad m = +1, 0, -1 \tag{2.18}$$

where m labels the spin component, and $\mathbf{k}$ are harmonic wave vectors of the box:

$$\mathbf{k} = \frac{2\pi}{L}(i, j, k) \qquad \text{i,j,k, integers} \tag{2.19}$$

2.2.2 Excitations

Keeping in mind that we'll be looking at non-equilibrium dynamics later, we'll need to look at the excitation spectrum first to determine what we expect to see, and where the instabilities should be.

In considering the excitation spectra, we take the second-order Hamiltonian and diagonalize it by utilizing the Bogoliubov approximation (where we replace zero-momentum operators with the particle number[6])

$$\begin{aligned} \hat{a}_0 &\to \sqrt{N_0} \\ \hat{a}^\dagger_{0,m}\hat{a}_{0,m'} &\to N_0 \psi^\dagger_m \psi_{m'} \\ \hat{a}^\dagger_{0,m_1}\hat{a}^\dagger_{0,m_2}\hat{a}_{0,m_2'}\hat{a}_{0,m_1'} &\to N_0(N_0-1)\psi^\dagger_{m_1}\psi^\dagger_{m_2}\psi_{m_2'}\psi_{m_1'} \end{aligned} \tag{2.20}$$

[6] This is valid in the low-temperature case as the condensate is very close to being in a coherent state, where the annihilation operator acting on a state is the same as that state being multiplied by some constant number.

and the Bogoliubov transformation[20]

$$\hat{a}_{\mathbf{k},m} = \sum_{m'} (u_{\mathbf{k},mm'}\hat{b}_{\mathbf{k},m'} + v_{-\mathbf{k},mm'}\hat{b}^\dagger_{-\mathbf{k},m'}) \tag{2.21}$$

Here, $\hat{b}$ and $\hat{b}^\dagger$ are the *quasiparticle operators* that destroy and create excitations (a "quasiparticle"), respectively. N_0 is the condensate particle number, and m denote the spin components.

Our quenching studies will look at quenching from at $p = 0$, $q \sim$ large polar phase, so we will look at the Bogoliubov dispersion spectra around the polar state. This leads to the Hamiltonians:

$$\mathbf{H}^{(0)} = \begin{pmatrix} \epsilon_{\mathbf{k}} - p + q + g_s n & 0 & 0 \\ 0 & \epsilon_{\mathbf{k}} + g_n n & 0 \\ 0 & 0 & \epsilon_{\mathbf{k}} + p + q + g_s n \end{pmatrix} \tag{2.22}$$

$$\mathbf{H}^{(2)} = \begin{pmatrix} 0 & 0 & g_s n \\ 0 & g_n n & 0 \\ g_s n & 0 & 0 \end{pmatrix} \tag{2.23}$$

where $n = N_0/L^3$ is the number density and $\epsilon_{\mathbf{k}} = \hbar^2\mathbf{k}^2/(2m)$ the kinetic energy.

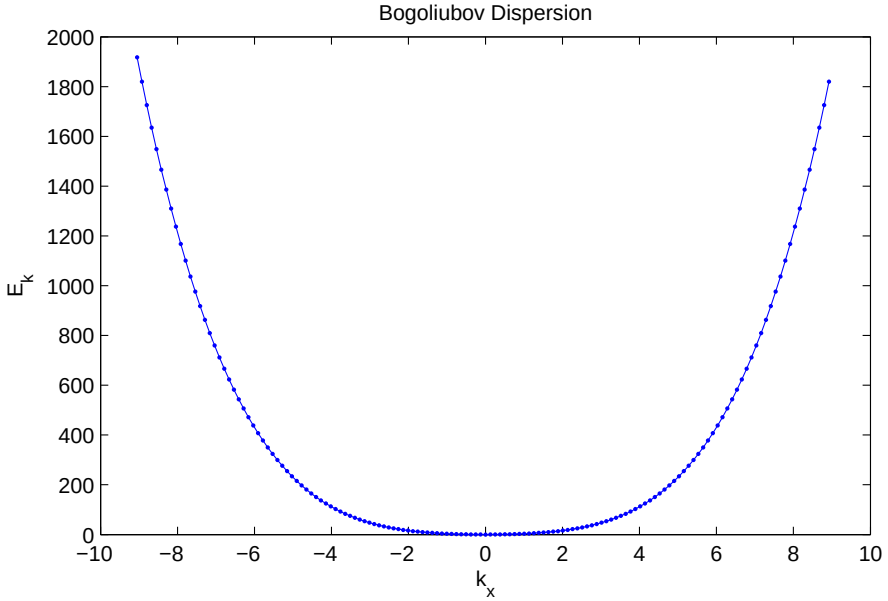

Figure 2.8: The Bogoliubov dispersion spectrum. Note that at low k values, the dispersion is linear and behaves like a phonon. At higher k it reaches the free-particle regime.

Solving the Bogoliubov-de Gennes equation[21] for the above matrices gives us the spectrum with three branches. The density ($m = 0$) branch gives famous scalar Bogoliubov dispersion (plotted in Fig. 2.8):

$$E_{\mathbf{k},0} = \sqrt{\epsilon_{\mathbf{k}}(\epsilon_{\mathbf{k}} + 2g_n n)} \tag{2.24}$$

which is phonon-like at low k; i.e., $E_{\mathbf{k}}, 0 \approx c\mathbf{k}$, where c is the density speed of sound. This branch is the Nambu-Goldstone mode associated with $U(1)$ symmetry breaking. This is accompanied by two other spin branches:

$$E_{\mathbf{k},\pm 1} = \sqrt{(\epsilon_{\mathbf{k}} + q)(\epsilon_{\mathbf{k}} + q + 2g_s n)} \mp p \tag{2.25}$$

arising from population transfers between the $m = 0$ and $m = \pm 1$ states. Taking $p = 0$ and $0 \leq q \leq 4|g_s|n$, we plot the real and imaginary components of the dispersion spectrum:

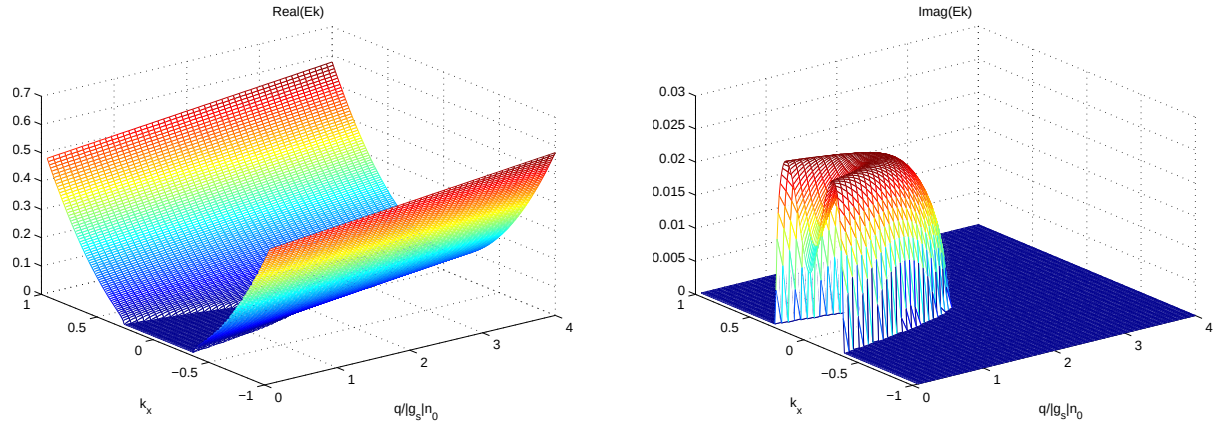

Figure 2.9: Real and imaginary components of the Bogoliubov dispersion relation for spin mixing modes, where the z axis is E_k

It is important to note here that the rise of non-zero imaginary values point to exponentially growing unstable states within the system[7] — the system becomes unstable here. If one would recall the form of a stationary state:

$$|\varphi(t)\rangle = e^{-iE_\varphi t/\hbar}|\varphi(0)\rangle$$

that evolves with a phase $E_\varphi t/\hbar$ given by the dispersion spectrum for some k. When this energy becomes imaginary, the argument of the exponential function becomes real and hence an instability is formed — the mode $|\varphi(0)\rangle$ grows, or decays, exponentially with time.

Thus, taking a polar state into the region where $\mathrm{Im}(E_k) \neq 0$ (that is, $q < 2|g_s|n$, as in Fig. 2.9), we are essentially pulling the ground out from underneath our system. This can be done by suddenly *quenching* the magnetic field to a smaller quadratic Zeeman. The polar state now sits atop the peak of an instability, and must fall into its new ground state. This instability is what we will be investigating later on.

2.2.3 Healing Lengths

Recall the Bogoliubov dispersion relation for the $U(1)$ symmetry-broken mode in Fig. 2.8. For slow momenta; i.e., $\hbar k \ll mc = \sqrt{mg_n n}$, we enter a phonon dispersion regime, and quantum fluctuations dominate the excitations. However, for large momenta, the dispersion reaches a free-particle form:

$$E_{\mathbf{k}} = \frac{\hbar^2 \mathbf{k}^2}{2m} + g_n n$$

where particle-particle interactions dominate.

The transition between the two regimes occurs when the density interactions are comparable to its kinetic energy. This happens at $\hbar^2 k^2/2m = g_n n$, and gives as a nice characteristic length over which the condensate responds to density perturbations. Taking $k = 1/\xi_n$, we define the condensate *healing length* as

$$\xi_n = \sqrt{\frac{\hbar^2}{2mg_n n}} \tag{2.26}$$

This is the length scale at which we can perturb our condensate and still have it 'heal' back to its original value.

Similarly, we can define a *spin healing length*, which is the length scale over which spin dependent interactions equate to kinetic energy.

$$\xi_s = \sqrt{\frac{\hbar^2}{2m|g_s|n}} \tag{2.27}$$

When simulating spin dynamics, we must ensure that our condensate is much larger than the spin healing length if we are to resolve those dynamics[7].

[7] In saying that, if we limit our condensate so it's smaller than its spin healing length, we observe population transfers between the $m = 0$ and $m = \pm 1$ states that oscillate back and forth, as we'll see in the next section.

2.3 Spin Dynamics

2.3.1 Quasi-2D Condensates

Notice that in the previous section the spinor GPEs (2.15) were derived for the three-dimensional case, while we are working with two-dimensional condensates.

In experiment, we can create a quasi-2D condensate by upping the axial trapping frequency so that the condensate is squeezed in the z direction into a pancake shape. When the length of the condensate in the z direction is smaller than the spin and particle healing lengths, all interactions are effectively frozen in that direction, and we can treat the gas as a purely 2D condensate.

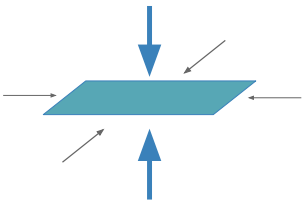

Figure 2.10: A quasi-2D condensate and its relative trapping frequencies.

Given the dynamics along the z axis remains frozen, we can separate out the z component of the wavefunction

$$\Psi^{(3D)}(x, y, z, t) = \Psi^{(2D)}(x, y, t)\chi(z)$$

where $\chi(z)$ is the harmonic oscillator ground state in the z direction.

Plugging this form of the wavefunction back into the spinor GPEs, it's a simple exercise to show that the z dependence can be integrated out except for the interaction terms. Due to the axial direction being assumed weak compared to the z confinement, the condensate is simply in the harmonic oscillator ground state in that direction. Continuing with our integration exercise we find that the effective two-dimensional interaction parameter is given by

$$g^{(2D)} = \frac{g^{(3D)}}{\sqrt{2\pi} l_z}, \tag{2.28}$$

where l_z is the harmonic oscillator length in the z direction, given by

$$l_z = \sqrt{\frac{\hbar}{m\omega_z}} \tag{2.29}$$

From now on we will omit the (2D) superscript and work exclusively with the 2D interaction parameter.

2.3.2 Non-equilibrium Spin Mixing

For a tightly confined BEC where the size of the condensate is smaller than the spin healing length, it is energetically costly for spatial spin textures to form. Thus, all components tend to share the same spatial wavefunction.

Thus we can break the order parameter up into spatially dependent (but spin independent) term, multiplied by a simple three-component spinor $\gamma(t)$:

$$\Psi = \Phi(r)\gamma(t) \tag{2.30}$$

where

$$\gamma(t) = \begin{pmatrix} \sqrt{\rho_+}e^{i\theta_+} \\ \sqrt{\rho_0}e^{i\theta_0} \\ \sqrt{\rho_-}e^{i\theta_-} \end{pmatrix} \tag{2.31}$$

This is known as the single-mode approximation (SMA), and considerably simplifies the spinor GPEs. Under the constraint of number and magnetization conservation, there are just two dynamical variables[22]: ρ_0, the fractional population of the $m = 0$ component, and relative phase difference $\theta(t) \equiv \theta_+ + \theta_- - 2\theta_0$. θ can be thought of as a control for the degree of magnetization.

Under the SMA, the spin-dependent energy functional is given by[23]:

$$E_s = g_s n \rho_0 [(1-\rho_0) + \sqrt{(1-\rho_0)^2 - M^2}\cos\theta] + q(1-\rho_0) \tag{2.32}$$

from which we can obtain the equations of motion for coherent dynamics:

$$\dot{\rho}_0 = -\frac{2}{\hbar}\frac{\partial E_s}{\partial \theta} \sim \text{const.} \times \sin\theta \tag{2.33}$$

$$\dot{\theta} = \frac{2}{\hbar}\frac{\partial E_s}{\partial \rho_0} \sim \text{const.} \times \cos\theta \tag{2.34}$$

A condensate that is smaller than the spin healing length, when allowed to evolve freely, displays coherent spin oscillations[24] in two distinct regimes along the quadratic Zeeman parameter, q. For clarity we take $p = 0$ and thus $M = 0$.

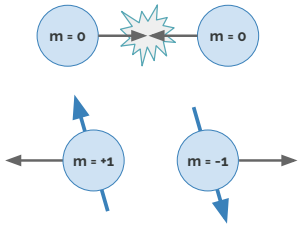

Figure 2.11: Schematic of spin mixing process.

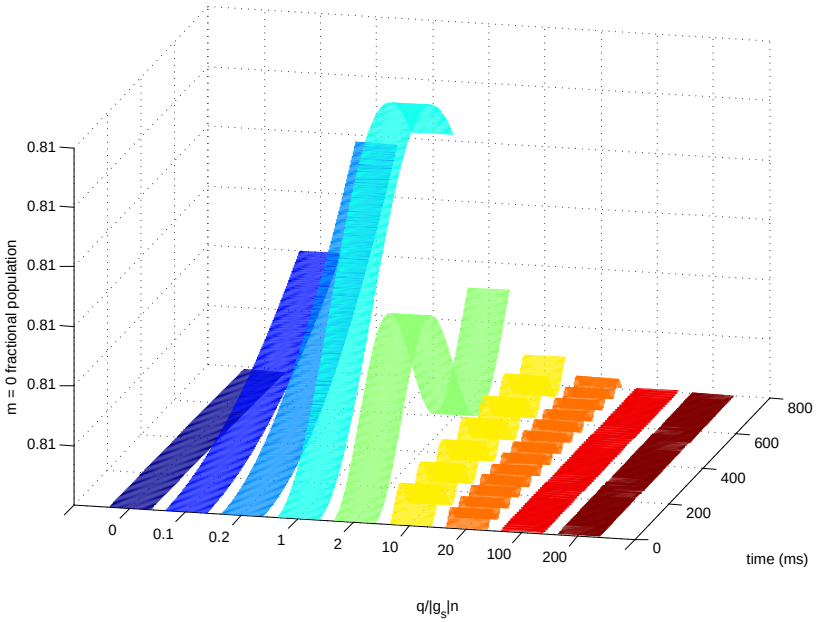

Figure 2.12: MATLAB simulation of spin oscillations at varying quadratic Zeeman. Note the resonance region around $q = |g_s|n$. Simulation parameters given in Chapter 4.

Along the quadratic Zeeman is a tug-of-war between the relative energies associated with the quadratic Zeeman shift and the spin-dependent interaction. In the interaction regime ($q \ll |g_s|n$), the g_s term in equation 2.32 dominates and interaction energies pull down the $m = \pm 1$ states. Here,

interaction-driven spin mixing prevails. In the Zeeman regime ($q \gg |g_S|n$), the $q(1-\rho_0)$ term dominates, the quadratic Zeeman effect lifts the energy of the $m = 0$ state and the amplitude of spin oscillations dampen at a rate of $1/q$[25].

In between the two extremes is where the spin interaction and quadratic Zeeman energies balance. Here the condensate reaches a "spin-mixing resonance"[26].

When SMA doesn't apply ($\xi_s < L$), the density and spin degrees of freedom are *spatially activated*. So when this is the case, what happens when we quench through this multicritical point?

2.3.3 Quenched Condensates

Classical systems quenched across a symmetry-breaking phase transitions have been well studied in the context of phase transitions in the early universe[2] and in low-temperature superfluids[1]. With the rise of experimentally viable $T \approx 0$ condensates, this treatment was naturally extended to a purely quantum phase transition (where we only consider quantum fluctuations and ignore thermal effects).

Recall how in Sec. 2.2.2 we found a region of instabilities for a spinor condensate in the polar ($\Psi_0 = (0,1,0)^{\mathrm{T}}$) state below $q = q_0 = 2|g_s|n$. This can be seen even more explicitly using Eq. (2.32) from the previous section: when we lower the quadratic Zeeman into the interaction regime, Eq. (2.32) displays an energy maxima — this is the dynamically unstable hilltop on which the current polar state sits, waiting to be pushed off by even the smallest of fluctuations. This dynamical instability was first noticed when, during numerical simulations of spin-mixing dynamics, Pu *et al.*[28] saw an unusually high sensitivity to noise. Ergo we can think of instabilities as amplifiers for infinitesimal quantum fluctuations.

We consider the influential Berkeley experiment[27], where Sadler *et al.* experimentally quench a spinor condensate through the multicritical point discussed previously, and, through the magic of *in situ* magnetization imaging, watched the growth of unstable modes manifest themselves in the form of spin domains.

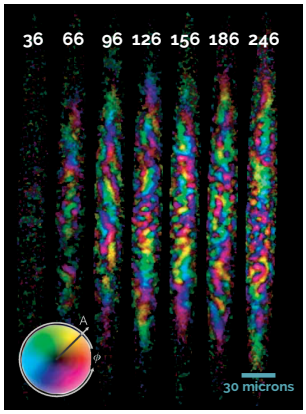

Figure 2.13: Sadler *et al.*'s *in situ* images of a quenched spinor condensate. Colored domains show the transverse (in-plane) magnetization, while the numbers above indicate time after quench in milliseconds. Source: [27]

On the effects of quench depth

In the Berkeley experiments the initial condensate starts well into the Zeeman regime ($q_i > q_0$). Short time dynamics show an exponential growth in transverse magnetization with time constant[29]

$$\tau = \frac{\hbar}{\sqrt{2mg_sn}} \tag{2.35}$$

Theoretical work by Lamacraft[7] showed the spectrum of unstable modes for deep quenches ($q_f \approx 0$) is

$$-E_{\mathbf{k}}^2 = \epsilon_{\mathbf{k}}(q_0 - \epsilon_{\mathbf{k}}) \tag{2.36}$$

which is maximized by $\mathbf{k} = \sqrt{q_0}$. This points to the growth of spin textures on the scale of $\sim \sqrt{q_0}$.

For shallow quenches ($q_f \approx q_0$), the unstable mode spectrum is given by:

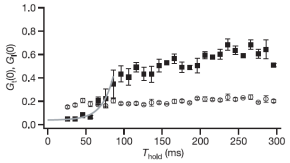

Figure 2.14: Measurements of growth in transverse magnetization over time. Source: [27]

$$-E_{\mathbf{k}}^2 = c_s^2(k_c^2 - \mathbf{k}) \tag{2.37}$$

It has been predicted that the condensate exhibits a peculiar 'light cone' growth in magnetization, akin to spin instabilities found in relativistic physics[30]. Here, $c_s \equiv q - q_0/2$ is the speed of sound for magnons (spin excitations), and $k_s \equiv -q(q - q_0)/c_s^2$. k_s is known as the *Compton wave vector* in scattering theory, and is equivalent to the wave vector of a photon whose energy is the same as the rest mass of the particle.

The border between the two extremities occurs at precisely $q = q_0/2$.

Correlation Functions

Though we can see qualitatively what happens after a quench through q_0, we need a quantitative way to measure the spin textures that appear — exactly how strongly magnetized are these domains? How large?

We hence turn our attention to correlation functions. In the most general sense, correlation functions are a measure of *order*. For example, if one wanted to know how ordered the spinors were in a condensate, one might look at a single spinor at position r. One then looks at all its neighbours at $r + dr$ and how similar they are — how much they correlate with the original spinor. Then one looks at a ring of spinors slightly further away, at $r + 2dr$. And then at $r + 3dr$, and $r + 4dr$, and so on, until all spinors have been compared to the original.

If we go through this process for every single point and average the results, we've just constructed the spatial correlation function.

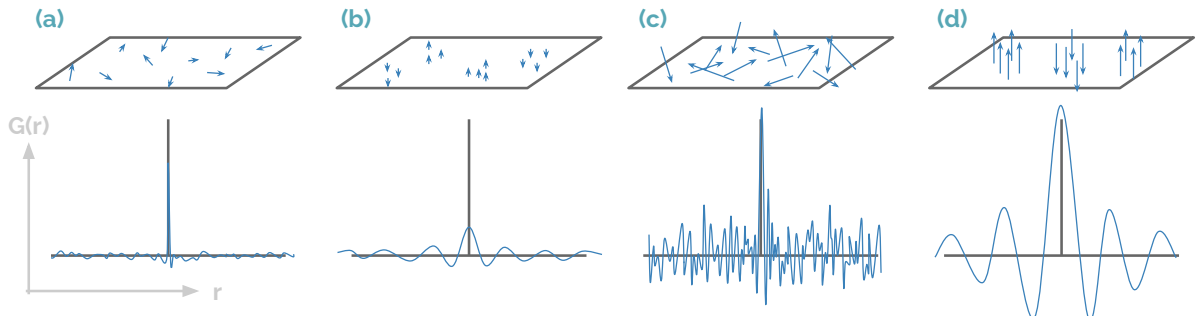

Figure 2.15: A qualitative overview of spatial correlation functions and how they indicate domain size and magnetization. (a) and (b) are closer to the polar phase, while (c) and (d) are strongly magnetized. However, in (a) and (c) the spinors are randomly oriented (indicated by the near-zero width of the central peak), while (b) and (d) have formed domains (indicated by the less noisy, sinc-like structure of the correlation function).

Formally, the spatial correlation function for transverse magnetization is given by

$$G_\perp(\mathbf{r}) = \frac{1}{n^2}\mathrm{Re}\left[\int d\mathbf{r} F_-(\mathbf{0})F_+(\mathbf{r})\right] \tag{2.38}$$

and the longitudinal correlation function

$$G_z(\mathbf{r}) = \frac{1}{n^2}\int d\mathbf{r} F_z(\mathbf{0})F_z(\mathbf{r}) \tag{2.39}$$

When we compute these values, it is much easier to utilize Fourier transforms:

$$G_\perp(\mathbf{r}) = \frac{1}{n^2}\mathrm{Re}\left[\mathcal{F}^{-1}\left(\mathcal{F}(F_+)\right) \times \left(\mathcal{F}(F_-)\right)\right] \tag{2.40}$$

where $\mathcal{F}$ is the 2D Fourier transform, and $F_\pm$ are given by Eq. (2.6).

Furthermore, we can look at the temporal dependence of spatial correlations — how much does our condensate change in time? Using Bogoliubov theory, these can be calculated for a $q_f = 0$ quench[8]:

$$G_\perp(t) = \frac{1}{\sqrt{8\pi q_0 t/\hbar}} \frac{1}{n\xi_s^2} e^{q_0 t/\hbar} \tag{2.41}$$

$$G_z(t) = \frac{1}{8^2 \pi q_0^2 t^2/\hbar^2} \frac{1}{(n\xi_s^2)^2} e^{2q_0 t/\hbar} \tag{2.42}$$

Plotting (2.41) and (2.42), we observe an exponential growth of magnetization following the quench, before reaching a plateau (See Fig. 2.16).

This begs the question: are we seeing the system thermalize?

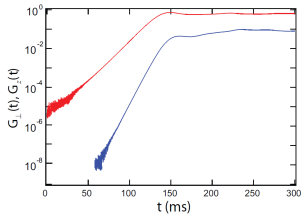

Figure 2.16: Plot of equations (2.41) and (2.42).

2.3.4 The Prospect of Thermalization

Though the thermalization properties of a system is of fundamental importance, relaxation dynamics in quantum systems still remains elusive. The question becomes even more complex in systems that cannot take easy routes to thermal equilibrium due to conservation constraints. Though we have quantum ergodic theory to tell us the requirements for a system to thermalize[31], the time scales at which this should happen is still ambiguous.

It was 2011 when Barnett *et al.*[8] conducted an investigation into long-time dynamics of the quenched spinor condensate. Due to the curve seen in Fig. 2.16, thermalization was first assumed, and theory for long-time behavior developed. Comparing this to their simulations, they found an irreconcilable difference: the decay of the spatial correlation function disagreed with their theory assuming thermalization. Hence it was concluded that the system instead reached a *prethermalized* state.

Prethermalization is an intriguing phenomenon characterized by an initial, quick establishment of some quasi-steady state. Thermal equilibrium, if it existed at all, occurs much later.

2.4 Summary

In this chapter we have covered the fundamental concepts of spinor condensates; its intrinsic properties, interactions, and phases. We introduced the spinor Gross-Pitaevskii equations, which will be used later on to simulate a spinor condensate. A light treatment of Bogoliubov theory was charted, with a focus on the dispersion relations of the polar phase. Along the way we touched on important concepts and quantities of our system: quasi-2D condensates, the particle and spin healing lengths, and spontaneous symmetry breaking. In spin dyanmics we learned about coherent spin-mixing and spin oscillations; the Zeeman and interaction regimes along q, and investigations into quench dynamics and thermalization.

2.4.1 Topic of this Thesis

In this thesis we focus exclusively on quenching ferromagnetic ^{87}Rubidium through the multicritical point $q_0 = 2|g_s|n$, keeping $p = 0$. We begin by

developing MATLAB code to efficiently and accurately simulate a spinor system. Thorough checks are made every step of the way – from simulating pure, uniform systems to reproducing the results of Barnett *et al.*'s paper. We then perform further investigations around quenching depths, and their long-time ramifications.

Chapter 3

Code Development

In this chapter we cover the numerical essentials behind our simulations. Though we are somewhat spoiled with the advent of affordable and accessible computing facilities, one must always make the most of it by developing the most efficient and accurate code possible. Here we discuss the importance of working in dimensionless variables, and the development of our Runge-Kutta algorithm for c-field methods. Not forgetting about the real world, we move on to consider experimentally viable parameters for two-dimensional spinor systems, and how to appropriately translate those to our simulations.

3.1 Dimensionless Formalism

In physics we work with units on a range of values orders of magnitude apart. This is not always favorable in a computational environment as we lose accuracy and efficiency when dealing with such a range. Hence we work in dimensionless units: expressing our variables in terms of chosen "natural units" for our system brings our parameters closer to unity.

In the following simulations we adopt the following natural units:

$$x = \bar{x} l_z \qquad t = \bar{t} \omega_z^{-1} \tag{3.1}$$

$$l_z = \sqrt{\frac{\hbar}{m\omega_z}} \tag{3.2}$$

where the barred variable is the dimensionless parameter, w_z is the trap frequency in the z direction, and l_z the harmonic oscillator length in the z direction.

It is worth noting here that the wavefunction has units of inverse length in 2D; hence,

$$\psi = \bar{\psi} l_z^{-1} \tag{3.3}$$

Substituting the above into the two-dimensional spinor GPEs, we obtain their dimensionless forms:

$$i\frac{\partial\bar{\psi}_+}{\partial\bar{t}} = \left[-\frac{\bar{\nabla}^2}{2} + \bar{g}_n^{(2D)}|\bar{\Psi}|^2 + \bar{g}_s^{(2D)}(|\bar{\psi}_+|^2 + |\bar{\psi}_0|^2 - |\bar{\psi}_-|^2)\right]\bar{\psi}_+ + \bar{g_s}^{(2D)}\bar{\psi}_-^\dagger\bar{\psi}_0^2 \tag{3.4a}$$

$$i\frac{\partial\bar{\psi}_0}{\partial\bar{t}} = \left[-\frac{\bar{\nabla}^2}{2} + \bar{g}_n^{(2D)}|\bar{\Psi}|^2 + \bar{g}_s^{(2D)}(|\bar{\psi}_+|^2 + |\bar{\psi}_-|^2)\right]\bar{\psi}_0 + 2\bar{g_s}^{(2D)}\bar{\psi}_-\bar{\psi}_0^\dagger\bar{\psi}_+ \tag{3.4b}$$

$$i\frac{\partial\bar{\psi}_-}{\partial\bar{t}} = \left[-\frac{\bar{\nabla}^2}{2} + \bar{g}_n^{(2D)}|\bar{\Psi}|^2 + \bar{g}_s^{(2D)}(|\bar{\psi}_-|^2 + |\bar{\psi}_0|^2 - |\bar{\psi}_+|^2)\right]\bar{\psi}_- + \bar{g_s}^{(2D)}\bar{\psi}_+^\dagger\bar{\psi}_0^2 \tag{3.4c}$$

By dimensional analysis we find the dimensionless 2D interaction parameters are given by

$$\bar{g}^{(2D)} = \frac{m}{\hbar^2}g^{(2D)} \tag{3.5}$$

where $g^{(2D)}$ is given in Sec. 2.3.1.

From now on we will omit the bars for simplicity.

3.2 The Projected Gross-Pitaevskii

Perhaps here is an appropriate place to further discuss visualising high and low energy "modes". When looking at excitations, it is useful to perform a Fourier transform and look at our system in k-space. The condensate is conveniently located at $k = 0$, while the higher energy modes are at, accordingly, higher k numbers.

When modes are macroscopically occupied, they can be simulated as classical fields. Hence the Projected Gross-Pitaevskii equation (PGPE) utilizes a projection operator that takes all the modes in the system and projects it onto a low-energy, coherent subspace[32], allowing us to simulate them using classical stochastic field equations. This subspace is defined by a parameter – ϵ_{cut} – which is explicitly chosen at the start of the simulation. Below ϵ_{cut} are all highly-Bose degenerate modes, including the condensate. We assume that the coupling to the incoherent region (of high-energy, sparsely occupied modes) is weak enough to be ignored.

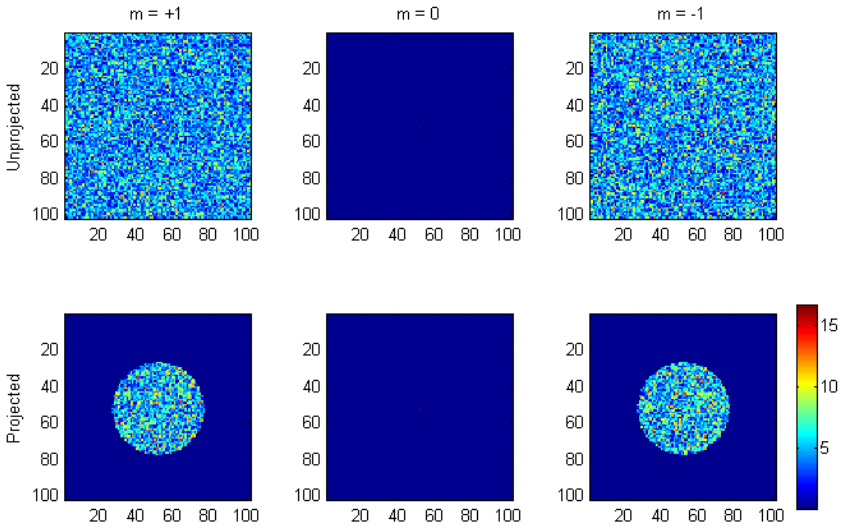

Figure 3.1: Projection operator in k-space. Note that there is a dark red spike at $k = 0$ in the $m = 0$ states, but it's hard to see.

Recall from Sec. 2.2.1 how we expanded our system in terms of plane

waves due to the periodic boundary conditions of our system:

$$\hat{\psi}_m = \frac{1}{\sqrt{L^2}} \sum_{\mathbf{k}} \hat{a}_{\mathbf{k},m} e^{i\mathbf{k}\cdot\mathbf{r}} \qquad m = +1, 0, -1 \tag{3.6}$$

Formally, the projection operator is defined as:

$$\hat{\mathcal{P}}\{f(\mathbf{x})\} = \sum_{|\mathbf{k}|<k_{\text{cut}}} \varphi_{\mathbf{k}}(\mathbf{x}) \int d^2\mathbf{x}' \varphi^*_{\mathbf{k}}(\mathbf{x}') F(\mathbf{x}') \tag{3.7}$$

where $f(\mathbf{x})$ is simply a spatially dependent function and φ are the single particle momentum states $\varphi_{\mathbf{k}} = \frac{1}{L} e^{i\mathbf{k}\cdot\mathbf{x}}$, and k_{cut} is the momentum-space cutoff corresponding to ϵ_{cut}.

In implementing this projector, we take the Fourier transform the spatial wavefunction into k-space, and then simply zero out all modes with $|\mathbf{k}| > k_{\text{cut}}$ (see Fig. 3.1). Now, in lieu of the rather complicated process in Eq. 3.7, we have

$$\hat{\mathcal{P}}\{\psi_m(\mathbf{x})\} = \mathcal{F}^{-1}(\hat{\mathcal{P}}_{\mathbf{k}}\{\mathcal{F}(\psi_m(\mathbf{x}))\}) \qquad m = +1, 0, -1 \tag{3.8}$$

where

$$\hat{\mathcal{P}}_{\mathbf{k}} = \begin{cases} 1 & \text{if } |\mathbf{k}| \leq k_{\text{cut}} \\ 0 & \text{if } |\mathbf{k}| > k_{\text{cut}} \end{cases} \tag{3.9}$$

We should also mention here that the PGPE decribes a *microcanonical system*; i.e., equilibrium is determined by the macroscopic quantities (energy, number and magnetization). Hence, those values are conserved quantities in our system.

3.3 Developing the VRKF45 Function

A significant proportion of this year's work was spent developing an efficient and accurate integration algorithm from scratch, in an attempt to gain a better grounding in numerical methods. To simulate a spinor condensate we must develop an algorithm to solve three coupled GPEs, given in their preprepared dimensionless forms in Eq. 3.4.

The Algorithm

The Runge-Kutta algorithm is a fourth order iteration of the general Euler method for advancing a solution from x_n to $x + h \equiv x_{n+1}$:

$$y_{n+1} = y_n + hf(x_n, y_n) \tag{3.10}$$

This gives a step error on the order of $O(h^2)$, where h is the step size and $f(x_n, y_n)$ is the derivative dy/dx. That's alright, but we can do better.

Let's consider the next level: what if we were to evaluate the derivative at a trial step somewhere between x and $x + h$, then use both values to construct the solution at $x + h$? This *second order* method gives an error of $O(h^3)$ – a little better.

As the reader may already guess, we can keep evaluating trial points between x and $x + h$ to get more and more precise solutions, but computational demand goes up linearly for each order we climb. Most stop at

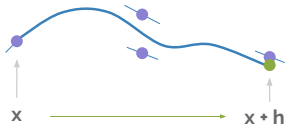

Figure 3.2: The fourth-order Runge-Kutta algorithm for propagating a function forward by step h. Derivative evaluations are given by purple dots; the final answer by a green dot.

fourth order, where we evaluate the derivative (see Fig. 3.2) at x, two at trial midpoints and another at $x + h$. We now get a solution with error term $O(h^5)$[1].

[1] Iit is here we must remind ourselves that *high order* does not equate to *high accuracy* — they may correlate, but one does not necessary lead to the other.

Adaptive Stepsize

Ideally what we want is an algorithm that gives us a solution to a preset accuracy, all while consuming the minimum amount of processing power. We want to take care during quickly-changing terrain, while flying past boring plains. To achieve this, we need an idea of how well we're doing; an estimate of the *truncation error*. Thus we evaluate the fourth *and* fifth order solutions for our problem. The fifth-order solution acts as a performance monitor, and its difference between the fourth one is what gives our truncated error. A big error means we need not be too hasty, while a small error allows us to take larger strides.

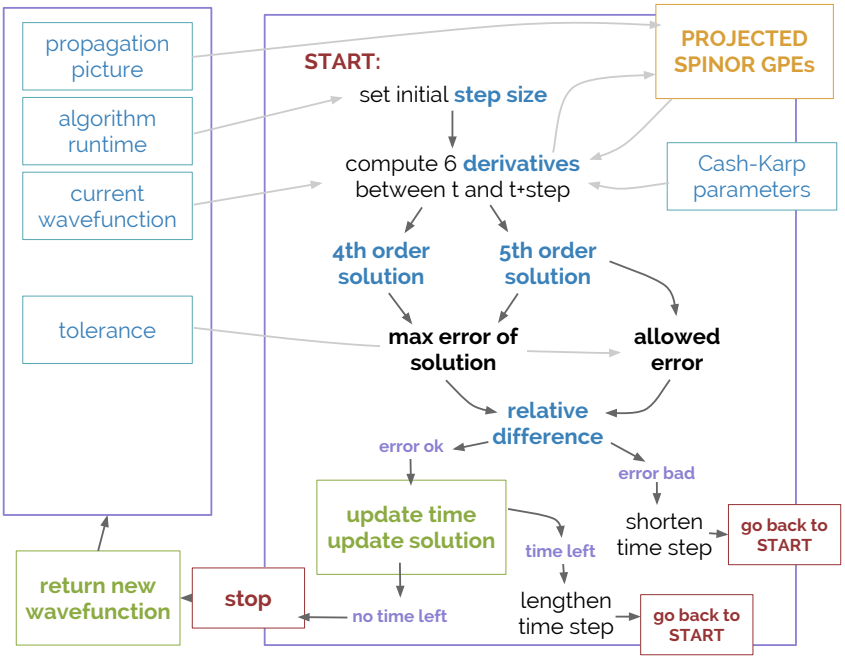

Figure 3.3: Overview of the Runge-Kutta algorithm used in this work. Diagram shows the relationship between the executable program (purple box, left) and the VRKF45 function file (purple box, right).

One may rightly ask at this point: what's stopping us from just using the fifth-order solution instead? Alas, we can't have any pudding if we don't eat our meat, and without a higher order solution to compute a truncation error, we cannot implement an adaptive stepsize.

Formally, the midpoint evaluations are given by[33]:

$$
\begin{aligned}
K_1 &= hf(x_n, y_n) \\
K_2 &= hf(x_n + \frac{h}{4}, y_n + \frac{1}{4}K_1) \\
K_3 &= hf(x_n + \frac{3}{8}h, y_n + \frac{3}{32}K_1 + \frac{9}{32}K_2) \\
K_4 &= hf(x_n + \frac{12}{13}h, y_n + \frac{1932}{2197}K_1 - \frac{7200}{2197}K_2 + \frac{7296}{2197}K_3) \\
K_5 &= hf(x_n + h, y_n + \frac{439}{216}K_1 - 8K_2 + \frac{3680}{513}K_3 - \frac{845}{4104}K_4) \\
K_6 &= hf(x_n + \frac{h}{2}, y_n - \frac{8}{27}K_1 + 2K_2 - \frac{3544}{2565}K_3 + \frac{1859}{4104}K_4 - \frac{11}{40}K_5)
\end{aligned}
\tag{3.11}
$$

From these, we obtain the fourth-order,

$$y_{n+1}^{(4)} = y_n + \frac{25}{216}K_1 + \frac{1408}{2565}K_3 + \frac{2197}{4104}K_4 - \frac{1}{5}K_5 \tag{3.12}$$

and fifth order solutions:

$$y_{n+1}^{(5)} = y_n + \frac{16}{135}K_1 + \frac{6656}{12825}K_3 + \frac{28561}{56430}K_4 - \frac{9}{50}K_5 + \frac{2}{55}K_6 \tag{3.13}$$

This algorithm is called the *Runge-Kutta-Fehlberg*, and will be the one we use.

It is here we wish to stress to the reader: our spinor system is more complex, with three individual, but coupled, components. The above values are not simply scalar — y_n, for example, is an $N \times N \times 3$ element vector representing the spinor. K_i is also an $N \times N \times 3$ element vector, representing the derivatives in the spinor GPEs. x_n, which we use as time, is a scalar.

Cash-Karp Parameters

All of the crazy coefficients you see in the above equations are the *Fehlberg coefficients*. Though satisfactory, there exists a more efficient method that performs better for differential equations with avidly fluctuating right-hand-sides[34]: the Cash-Karp parameters. a_i gives the coefficients in front of h, the timestep in Eq. (3.11), while b_{ij} gives the coefficients in front of the K_i values. $c_i^{(4)}$ and $c_i^{(5)}$ give the coefficients to construct the fourth and fifth order solutions, repsectively (see Eq. 3.12, 3.13).

a_i	b_{ij}					$c_i^{(4)}$	$c_i^{(5)}$
0	0	0	0	0	0	$\frac{37}{378}$	$\frac{2825}{27648}$
$\frac{1}{5}$	$\frac{1}{5}$	0	0	0	0	0	0
$\frac{3}{10}$	$\frac{3}{40}$	$\frac{9}{40}$	0	0	0	$\frac{250}{621}$	$\frac{18575}{48384}$
$\frac{3}{5}$	$\frac{3}{10}$	$-\frac{9}{10}$	$\frac{6}{5}$	0	0	$\frac{125}{594}$	$\frac{13525}{55296}$
1	$-\frac{11}{54}$	$\frac{5}{2}$	$-\frac{70}{27}$	$\frac{35}{27}$	0	0	$\frac{277}{14336}$
$\frac{7}{8}$	$\frac{1631}{55296}$	$\frac{175}{512}$	$\frac{575}{13824}$	$\frac{44275}{110592}$	$\frac{253}{4096}$	$\frac{512}{1771}$	$\frac{4}{4}$

Table 3.1: The Cash-Karp parameters for constructing the time step (a), derivatives (b), and the fourth/fifth order solutions (c).

In recalculating our stepsize inside the algorithm, we use the following relation[35]:

$$h_{\text{new}} = \begin{cases} S \times h_{\text{current}} \times |\frac{\text{Emax}}{\text{TE}}|^{0.20} & \text{if Emax } \geq \text{TE} \\ S \times h_{\text{current}} \times |\frac{\text{Emax}}{\text{TE}}|^{0.25} & \text{if Emax } < \text{TE} \end{cases} \tag{3.14}$$

where S is a safety factor, around about $\sim$ 92%. As stated before, the truncation error (TE) is given by the maximum difference between the fifth and fourth order solutions:

$$\text{TE} = \max(|y_{n+1}^{(4)} - y_{n+1}^{(5)}|) \tag{3.15}$$

and the allowed error, Emax, is defined as

$$\text{Emax} = \text{tolerance} \times \max(y_{n+1}^{(5)}) \tag{3.16}$$

where we harness a preset tolerance (usually on the order of $10^{-6}, 10^{-8}$). These are the parameters we'll be using in our algorithm; Fig. 3.3 gives a graphical overview of the whole shebang.

Initial testing against MATLAB*'s* ode45

In writing this new algorithm, we want to make sure that it is at least as good as MATLAB's bundled ode45. Though good for simple systems, MATLAB's ode45 function fails to propagate the GPEs accurately, mainly due to how it calculates error. Nevertheless, it provides us with a good starting ground to compare our baby code. Using the same tolerance settings for both algorithms, we study their performance with a simple harmonic oscillator model:

$$m\frac{d^2x}{dt^2} = -kx$$

This has the exact solution

$$x(t) = A\cos(\omega t + \theta)$$

Plotting the ode45 and VRKF45 solutions:

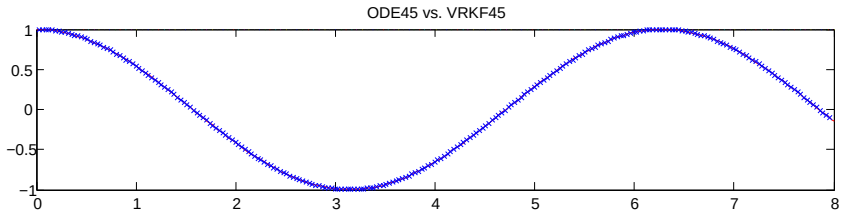

Figure 3.4: ODE45 (line) and VRKF45 (crosses) solutions for the simple harmonic oscillator.

Fig. 3.4 shows good agreement, but let's see exactly how well they're doing. Pitting the two against one another, we find that VRKF45 does well at a tolerance setting of 10^{-8}:

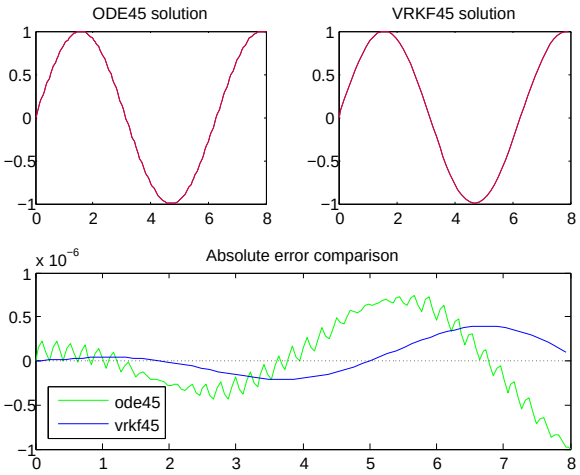

Figure 3.5: Absolute error comparison between ODE45 and VRKF45 solutions for a tolerance of 10^{-8}.

And even better at higher tolerances (this one is at 10^{-10}):

However, if we lower the tolerance to 10^{-6}, VRKF45 starts failing:

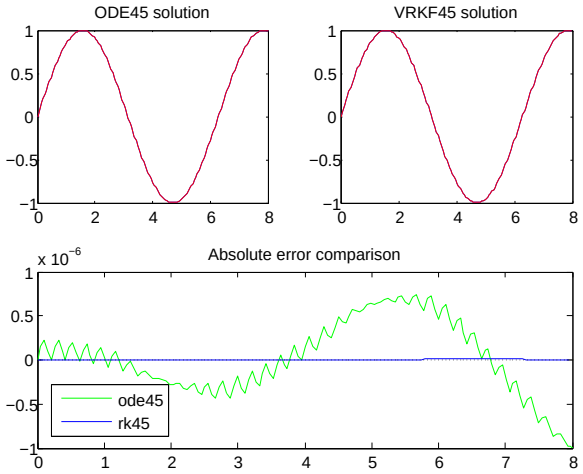

Figure 3.6: Absolute error comparison between ODE45 and VRKF45 solutions for a tolerance of 10^{-10}.

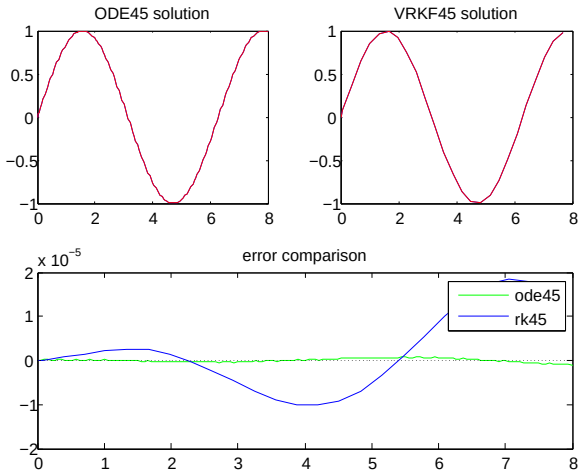

Figure 3.7: Absolute error comparison between ODE45 and VRKF45 solutions for a tolerance of 10^{-6}.

VRKF45 seems to be doing better, faster than ODE45 at high tolerances; and yet it does worse quicker as the tolerance is lowered. Our suspicion is that there's something off with the error calculations — perhaps they are more sensitive than they should be to tolerance settings. What we do know is that ode45 measures error differently, and how it does so is not completely documented. This is perhaps the reason ode45 fails to propagate the GPEs — it might be, for example, sensitive to phase errors.

Due to these results, we'll now exclusively work with a tolerance of 10^{-8} or higher.

3.3.1 Interaction Picture

In computing the derivatives for the VRKF45, we take our spinor GPEs into the interaction picture. This is useful, mostly because $\mathcal{H}_0$is relatively easy to solve, so we jam all of our time dependence onto our operators and let them evolve freely. Currently, the GPEs are in the form:

$$i\frac{\partial \psi_m}{\partial t} = (\hat{\mathcal{H}}_0 + \hat{\mathcal{H}}_{int_m})\psi_m \tag{3.17}$$

where $\hat{\mathcal{H}}_0 = k^2/2$ is the free (dimensionless) Hamiltonian, and $\hat{\mathcal{H}}_{int_m}$ the interaction Hamiltonians:

$$\mathcal{H}_{int_+} = \left(p + q + g_n|\Psi|^2 + g_s(|\psi_+|^2 + |\psi_0|^2 - |\psi_-|^2)\right)\psi_+ + g_s\psi_-^\dagger\psi_0^2 \quad (3.18a)$$

$$\mathcal{H}_{int_0} = \left(g_n|\Psi|^2 + g_s(|\psi_+|^2 + |\psi_-|^2)\right)\psi_0 + 2g_s\psi_-\psi_0^\dagger\psi_+ \quad (3.18b)$$

$$\mathcal{H}_{int_-} = \left(-p + q + g_n|\Psi|^2 + g_s(|\psi_-|^2 + |\psi_0|^2 - |\psi_+|^2)\right)\psi_- + g_s\psi_+^\dagger\psi_0^2 \quad (3.18c)$$

In the interaction picture, we transform the Schrödinger picture spinor (ψ_m) according to:

$$\psi_m^{(\mathbf{I})} = e^{i\mathcal{H}_0\frac{t}{\hbar}}\psi_m \quad (3.19)$$

for which the GPEs transform to:

The superscript (**I**)s denote the interaction picture version of the quantity.

$$\begin{aligned} i\frac{\partial\psi_m^{(\mathbf{I})}}{\partial t} &= \hat{\mathcal{H}}_{int_m}^{(\mathbf{I})}\psi_m^{(\mathbf{I})} \\ &= e^{i\mathcal{H}_0 t}\hat{\mathcal{H}}_{int_m}\psi_m^{(\mathbf{I})} \\ &= e^{i\mathcal{H}_0 t}\hat{\mathcal{H}}_{int_m}e^{-i\mathcal{H}_0 t}\psi_m \end{aligned} \quad (3.20)$$

Thus, in the interaction picture the field evolves only under the influence of $\mathcal{H}_{int}$

$$i\frac{\partial\psi_m}{\partial t} = \hat{\mathcal{P}}\{e^{i\mathcal{H}_0 t}\hat{\mathcal{H}}_{int_m}\hat{\mathcal{P}}\{e^{-i\mathcal{H}_0 t}\psi_m\}\} \quad (3.21)$$

By exactly exponentiating $\mathcal{H}_0$, we hope that solving the GPEs may be more efficient.

3.3.2 Noise Considerations

When passing through a symmetry-breaking phase transitions, it is the quantum fluctuations that determine the following dynamics of the condensate. To seed these fluctuations, we add noise to our initial state.

Previous work by Saito *et al.* investigated the effects of different noise profiles in a numerical reproduction of the Berkeley experiment[29]. In a study of no noise, white noise and colored noise, white noise produced results most like those of the Berkeley experiment. Hence it is white noise – i.e., random numbers obeying a normal distribution – that we will employ.

Adding noise is tricky business. To make sure we are adding in the right amount of noise, we utilize the truncated Wigner formalism.

The Truncated Wigner Representation

One may recall that our field operator $\hat{\Psi}$ fulfills the following commutation relation:

$$[\Psi(r), \Psi^\dagger(r)] = \Psi(r)\Psi^\dagger(r) - \Psi^\dagger(r)\Psi(r) = \delta(0) = \infty \quad (3.22)$$

Physically this infinity corresponds to vacuum fluctuations for the infinite number of excitation modes in a continuous system. Thankfully, this infinity is avoided through discretizing our system for numerical methods.

In the truncated Wigner representation, the mean atomic density of our condensate is expressed as follows[36]:

$$\langle\hat{\Psi}^\dagger\hat{\Psi}\rangle = \langle\Psi^*\Psi\rangle_w - \frac{1}{2}\langle[\hat{\Psi}, \hat{\Psi}^\dagger]\rangle \quad (3.23)$$

where $\langle \Psi^* \Psi \rangle_w$ is an average over the *Wigner function*; i.e., the semiclassical trajectories we simulate within the GPE. In a general sense, the Wigner function is a probability density in phase space[2], just like the wavefunction is in real space. However, the Wigner function is allowed negative values, making it a *quasi*-distribution function[3].

Note well that the $\frac{1}{2}$ term in Eq. (3.23) is *not* a part of the condensate density, but corresponds to the vacuum fluctuations as shown in Eq. (3.22). Thus the condensate field needs to have noise added to the real density to mimic these vacuum fluctuations. We need to add, on average, half an atom to each mode.

In implementing this, we have

$$\Psi = \sqrt{n_0} \begin{bmatrix} 0 \\ 1 \\ 0 \end{bmatrix} + \tilde{\Psi} \tag{3.24}$$

where $\tilde{\Psi}$ is our noise term, given for each excitation mode:

$$\tilde{\Psi} = \begin{pmatrix} \sum_k w_k \frac{1}{L} e^{ikx} \\ \sum_k w_k \frac{1}{L} e^{ikx} \\ \sum_k w_k \frac{1}{L} e^{ikx} \end{pmatrix} \tag{3.25}$$

To construct this, we make sure that the complex noise amplitudes w_k satisfy $\overline{|w_k|^2} = 1/2$. This noise can be equivalently added in position space as:

$$\tilde{\Psi} = \frac{1}{2l} \begin{pmatrix} \mathcal{R} + i\mathcal{R} \\ \mathcal{R} + i\mathcal{R} \\ \mathcal{R} + i\mathcal{R} \end{pmatrix} \tag{3.26}$$

Here, l is the lattice constant of our grid in real space, and $\mathcal{R}$ is the random number function that produces our white noise (Gaussian envelope, normalized to unity with a variance of 1). Note that each $\mathcal{R}$ in Eq. (3.26) are separate calls to the random-number function.

3.4 System Parameters

In this thesis we will investigate spinor dynamics in an $F = 1$, ^{87}Rb gas with mass and scattering lengths[37, 38]:

$$m = 86.909u = 1.4432 \times 10^{-25}\text{kg}$$
$$a_0 = 101.8a_B = 5.4505 \times 10^{-9}\text{m}$$
$$a_2 = 100.4a_B = 5.3129 \times 10^{-9}\text{m}$$

where u is the atomic mass and a_B is the Bohr radius.

3.4.1 Experimental Values and Grid Size

In purely numerical studies one must be careful that the parameters we use to simulate our system are realistically viable. In our code we implement the dimensionless aliases of parameters used in the Berkeley quenching experiments on quasi-2D spinor BECs.

[2] A probability density representation in phase space is super useful for those looking at coherent systems such as BECs. Vacuum modes are simply Gaussians centered around the origin, and a coherent state is simply the vacuum state translated somewhere else. It is also useful for seeing phenomena such as quantum squeezing; a direct manifestation of Heisenberg's Uncertainty Principle.

[3] Don't worry — this is not so paradoxical as one might think. Regions of negative probability cannot be larger than a few $\hbar$, and are shielded from measurements by the uncertainty principle.

Following the Berkeley experiments[39], we simulate quasi-2D condensates with an axial trapping frequency of $2\pi \times 440$ Hz, giving us a spin healing length of $\xi_s = 2.5\mu$m. We then discretize the system on a grid with lattice constant $l \ll \xi_s$ and $n_0 l^2 \gg 1$, all while the total grid size $L \gg \xi_s$. This is done to guarantee a large enough condensate to resolve spin textures, and yet small enough to lessen the computational demand.

In initializing this grid we chose a condensate size of $L = 50 = 25.7\mu$m with looped boundary conditions to simulate an essentially infinite 2D plane. An energy cutoff of $\epsilon_{cut} = 5\hbar\omega_z$ was chosen to give a lattice constant of $l = 0.25202\mu$m. Other used parameters are included in the table below.

Parameter	Value
n_0	800
L/l_z	50
$\epsilon_{cut}/\hbar\omega_z$	5
$\omega_z/2\pi$	440
l/l_z	0.4902
ξ_n/l_z	0.7022
ξ_s/l_z	7.591
$g_n^{(2D)}(\hbar^2/m)$	0.0369
$g_s^{(2D)}(\hbar^2/m)$	-0.000316

Table 3.2: Realistic parameters used for simulations. Note that these are all for a ^{87}Rb gas, and all parameters are given in the dimensionless forms. The smaller system was used for various code checks and witnessing spin-oscillations, while the larger system was used to see spontaneous magnetization. For our quenching runs we used the medium-sized system.

Chapter 4

Simulations

Here we observe the fruits of our labor, and use our newly developed code to simulate the spinor system. First, though, our code is run through some basic tests: does it conserve the constants of motion? Does its phase evolve as expected? We then attempt to reproduce previous work showing spontaneous magnetization and prethermalization. Moving onto more flavoursome territories, we investigate quenches at different depths, and its effect on domain formation. Results are discussed as they are presented.

4.1 The Uniform Spinor Condensate

As an initial exercise we evolve a uniform condensate using our developed code. We check that conservation laws are satisfied, as well as checking that the phase evolution and spin oscillations behave as expected.

The uniform condensate is also a good case to keep coming back to when one is debugging code for more complex situations later on.

4.1.1 Constants of Motion

Formally[40], the energy, number and overall magnetization (F_z) of a spinor BEC are conserved as it evolves. These quantities, defined as

$$E = \sum_{\substack{\text{all}\\ \text{x,y}}} \left(\frac{\hbar^2}{2m} |\nabla \Psi|^2 + V_{ext}(r)|\Psi|^2 + \frac{1}{2} g_n |\Psi|^4 + \frac{1}{2} g_s |\Psi^* \mathbf{F} \Psi|^2 \right) \Delta x \Delta y \quad (4.1)$$

$$N = \sum_{\substack{\text{all}\\ \text{x,y}}} \left(|\psi_+|^2 + |\psi_0|^2 + |\psi_-|^2 \right) \Delta x \Delta y \quad (4.2)$$

$$M = \sum_{\substack{\text{all}\\ \text{x,y}}} (F_z)\, \Delta x \Delta y = \sum_{\substack{\text{all}\\ \text{x,y}}} \left(|\psi_+|^2 - |\psi_-|^2 \right) \Delta x \Delta y \quad (4.3)$$

These come from the continuous expressions given by Yan and Ma (2012), and have been discretized for numerical calculation. Note that $\sum_{x,y} \Delta x \Delta y \simeq \int d\mathbf{r}$

where $\Psi = (\psi_+, \psi_0, \psi_-)^{\mathrm{T}}$, the full spinor wavefunction, and F_z the transverse magnetization.

Evolving a uniform, polar (i.e., $\Psi = (0, 1, 0)^{\mathrm{T}}$) condensate for the timescales we'll be looking at in our other simulations (~ 30 ms), we compute the relative errors of E, N and M, and observe good conservation up until the order of 10^{-12}. We present some examples as follows:

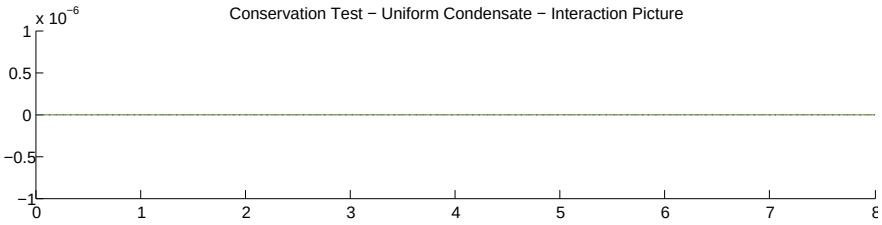

Figure 4.1: Relative deviation of the constants of motion from their initial values. $\Delta =$ (current)/(initial) $- 1$. Blue corresponds to magnetization, red to number, and green to energy.

In our simulations, we add noise to mimic quantum and thermal fluctuations in the system. As expected, this makes the conservation of energy a little worse:

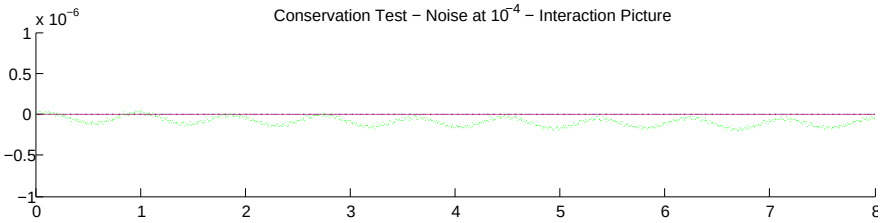

Figure 4.2: Relative deviation of the constants of motion, simulated with noise. Colors as in Fig. 4.1.

Note here that in Fig. 4.2 the condensate is evolved with the normal spinor GPEs. Using the PGPEs, we project out the higher-k modes created by the noise, and thus expect to see the constants of motion behaving a little better:

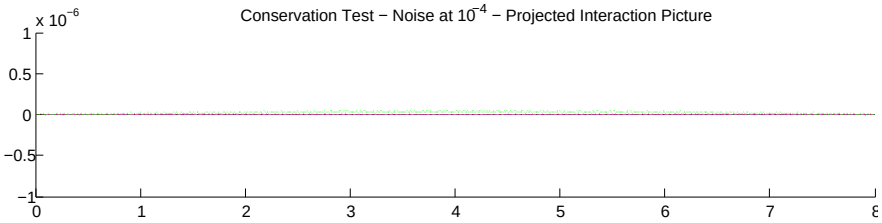

Figure 4.3: Relative deviation of the constants of motion with noise; simulated with the projected GPEs. Colors as in Fig. 4.1.

4.1.2 Phase Evolution

The phase evolution of a uniform spinor condensate can be quickly obtained with the spinor GPEs. For example, a uniform condensate entirely in the $m = +1$ component behaves as follows:

Because everything is in $m = +1$, $n = |\psi_+|^2$

$$i\hbar\frac{\partial\psi_+}{\partial t} = -\frac{\hbar^2}{2m}\nabla^2\psi_+ + g_n|\psi_+|^2\psi_+ + g_s(|\psi_+|^2)\psi_+ \tag{4.4}$$

with other component equations trivially zero. For a normalized, uniform condensate, we find that

$$\begin{aligned}\frac{\partial\psi_+}{\partial t} &= -\frac{i}{\hbar}(g_n + g_s)n\psi_+ \\ &= -\frac{i\mu}{\hbar}\psi_+ \qquad \text{where } \mu = (g_n + g_s)n\end{aligned}$$

$$\therefore \psi_+ = \sqrt{n}e^{-i\frac{\mu}{\hbar}t} \tag{4.5}$$

and thus the condensate evolves with a phase growing linearly in time

$$\phi = (g_n + g_s)n\frac{t}{\hbar} \tag{4.6}$$

Figure 4.4 shows the evolution of $\mathrm{Re}(\psi_+)$ with the parameters $g_n = 0.1$, and $g_s = -0.01$. By our calculations above we've plotted the expected evolution and the numerical one.

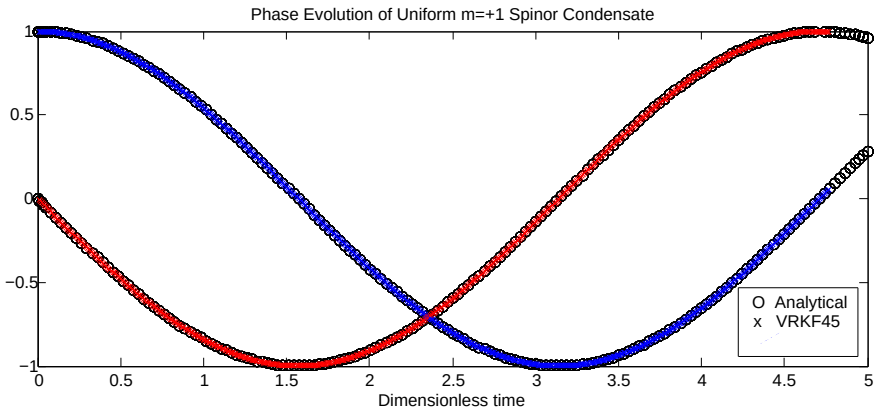

Figure 4.4: Comparison of the analytical (circles) and numerical (blue and red crosses) solutions for the phase evolution of a single component. Blue crosses plot the real component, red plots the imaginary component of phase ϕ.

4.1.3 Spin Oscillations

To see spin oscillations, we simulate a spinor system with a box length of $L \approx 1\mu m < \xi_s$, and a spatially uniform initial state of

$$\Psi = \begin{bmatrix} 0.05 \\ 0.9 \\ 0.05 \end{bmatrix}$$

The imperfect initial polar state is there to trigger the spin-exchange dynamics; empty $m = \pm 1$ components lead to no spin-exchanges within the GPEs; hence some seed is needed to initial the spin-mixing dynamics. Experimentally, due to quantum and thermal fluctuations, experiments observe spin oscillations even when the $m = \pm 1$ states are zero. The spin oscillations are due to the $\psi_+^\dagger \psi_-^\dagger \psi_0^2$ term in our Hamiltonian, which transfers $m = 0$ spinors to $m = \pm 1$ components.

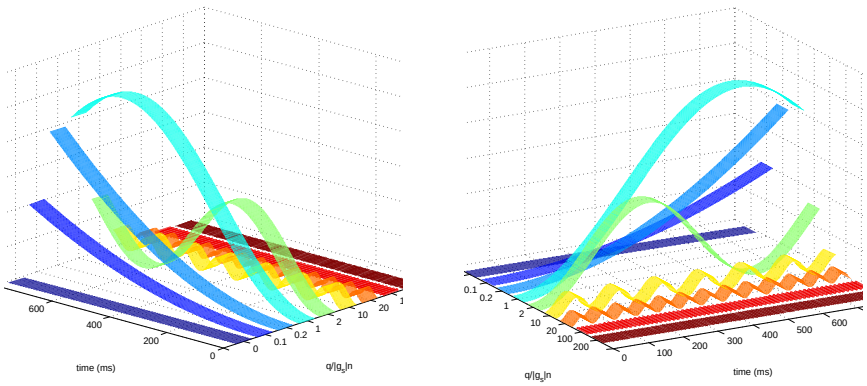

Figure 4.5: Spin oscillations of the $m = 0$ population at various q. (Left) focuses on the interaction regime, whereas (right) focuses on the damped oscillations in the Zeeman regime.

Fig. 4.5 reproduces the experimentally known phenomena of coherent spin-mixing between the polar $m = 0$ component and the $m = \pm 1$ components. If one will recall Sec. 2.3.2, inside the broken-axis phase there are two distinct spin-mixing regimes: the interaction ($q < |g_s|n$) and Zeeman ($q > |g_s|n$) parts. Kronjäger *et al.*[25] studied these spin oscillations, and found a "spin-mixing resonance" at $q = 1|g_s|n$, sucessfully reproduced by our code here.

4.2 Reproducing Prethermalization

Now that we have some confidence in our code, it's time to put it to the test: can it reproduce the results of Barnett *et al.*'s 2011 paper?

Here we use the simulation parameters given in Sec. **??** to generate our grids for simulating the full spinor system. Each m component of our spinor (which, here, is a 3D matrix) contains on the order of 100 elements, so when we propagate our system in time, we're actually solving $\sim 100^3$ coupled GPEs each iteration! Depending on how long we're propagating the system in realtime (usual around 25 to 100ms), a single run can take anything from half an hour two a week. The computational time is dependent on how simple (uniform) and large or system is, primarily. A lower energy cutoff in the projection operator can also help with improving computing times.

4.2.1 Spontaneous Magnetization

As we have learned before (Sec. 2.2.2), when we take a polar state into the interaction regime ($q < 2|g_s|n$), it becomes unstable and falls into the lower-energy, $m = \pm 1$ states. An observer looking at the transverse and longitudinal magnetization would see the system spontaneously form magnetized domains.

Let's see if our code can reproduce this effect. To first qualitatively see this, we simply start with a polar state with a low amount of noise to seed population-exchange interactions: $\Psi = [0, 1, 0]^{\mathrm{T}} + 10^{-8}(\mathcal{R} + i\mathcal{R})$, and interaction parameters $g_n = 1; g_s = -0.01$. Remember, we're dipping our toes in at this point. We're not worried about exact values, we just need to see if our code can give us something resembling a physical phenomena. Snapshots of transverse magnetizations F_x and F_y are shown in Fig. 4.7 (Printed on the following page).

Fig. 4.7 is very promising indeed — in this simulation, we see an exponential growth in transverse magnetization. Now let's get specific: time to implement the dimensionless versions of parameters from a real experiment, as given in Sec. 3.4:

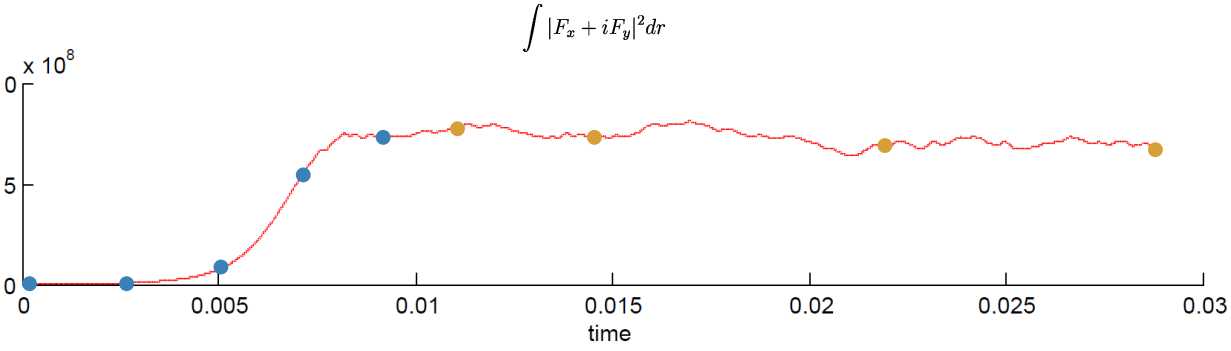

FIG. 4.8: Short-time dynamics

FIG. 4.9: "Coarsening"

Figure 4.6: Exponential growth of transverse magnetization. Dots indicate snapshots of F_x and F_y printed in this thesis: blue represents short-time dynamics of domain formation, while gold shows the condensate undergoing 'coarsening' — a topological phenomena that points to the condensate being in a prethermalized regime.

Fig. 4.6 shows the exponential growth of transverse magnetization, and when the snapshots in Fig.s 4.8 and 4.9 are taken. Fitting an exponential to this curve, we find that the time constant is $\approx$ 9ms.

We also notice that these spin domains seem to all have a characteristic domain width (which from now on we will denote d). A visual estimate of this domain size from Fig. 4.8 gives us a width of $\approx 7l_z \approx 7\mu$m.

4.2.2 Coarsening and Long-time Dynamics

Curiously, we've already started see prethermalization effects in our preliminary simulations. Fig 4.9 shows the well-formed domains grow and rip apart — the condensate no longer has a characteristic domain size, and we now see domains at a range of widths.

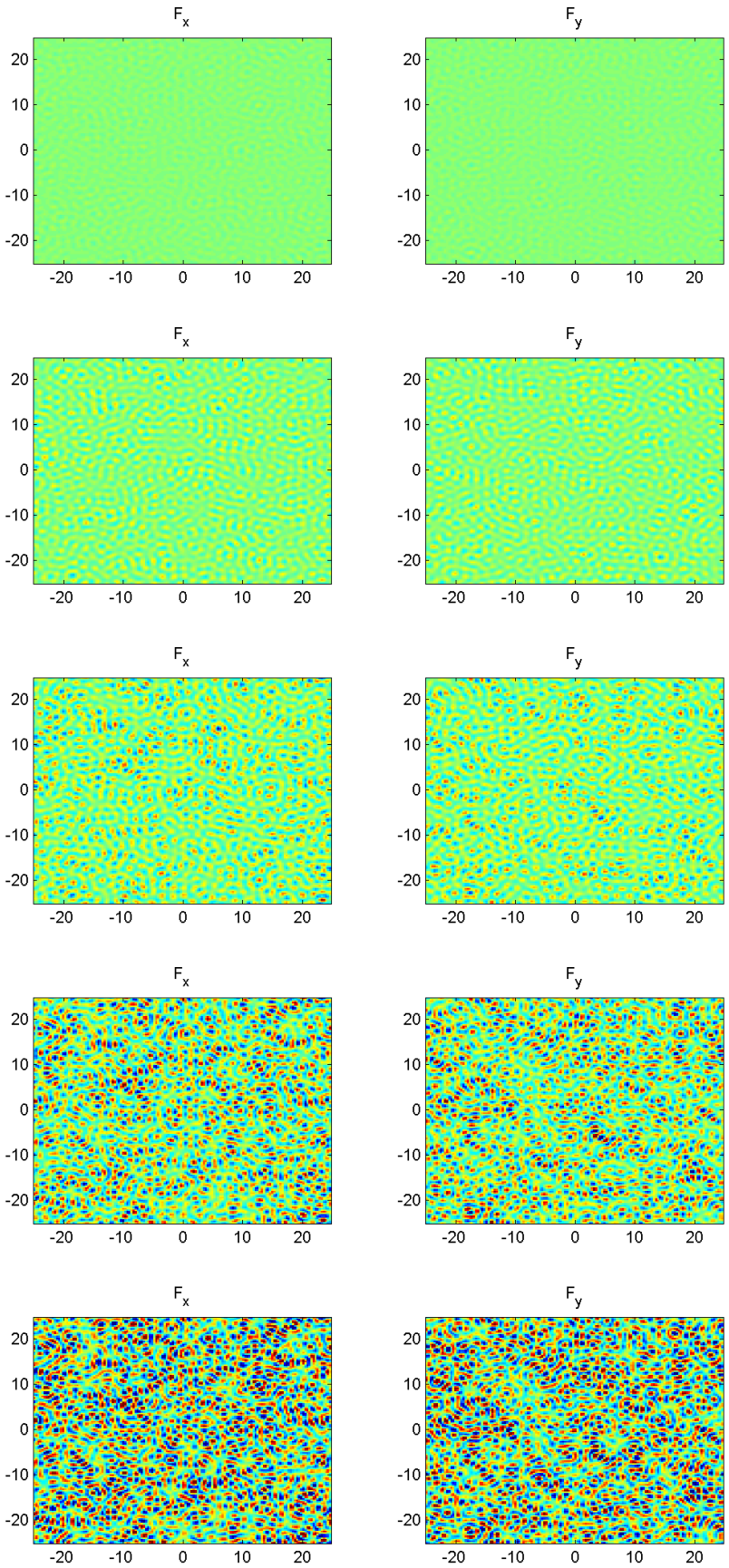

Figure 4.7: Qualitative run, observing spontaneous magnetization of a polar state at $p = 0$, $q = 0$ in the transverse directions, F_x (left), and F_y (right). x and y axes are real space positions with units l_z. Snapshots taken at $t = 0$, 8.3, 8.7, 9.1, 9.5ms.

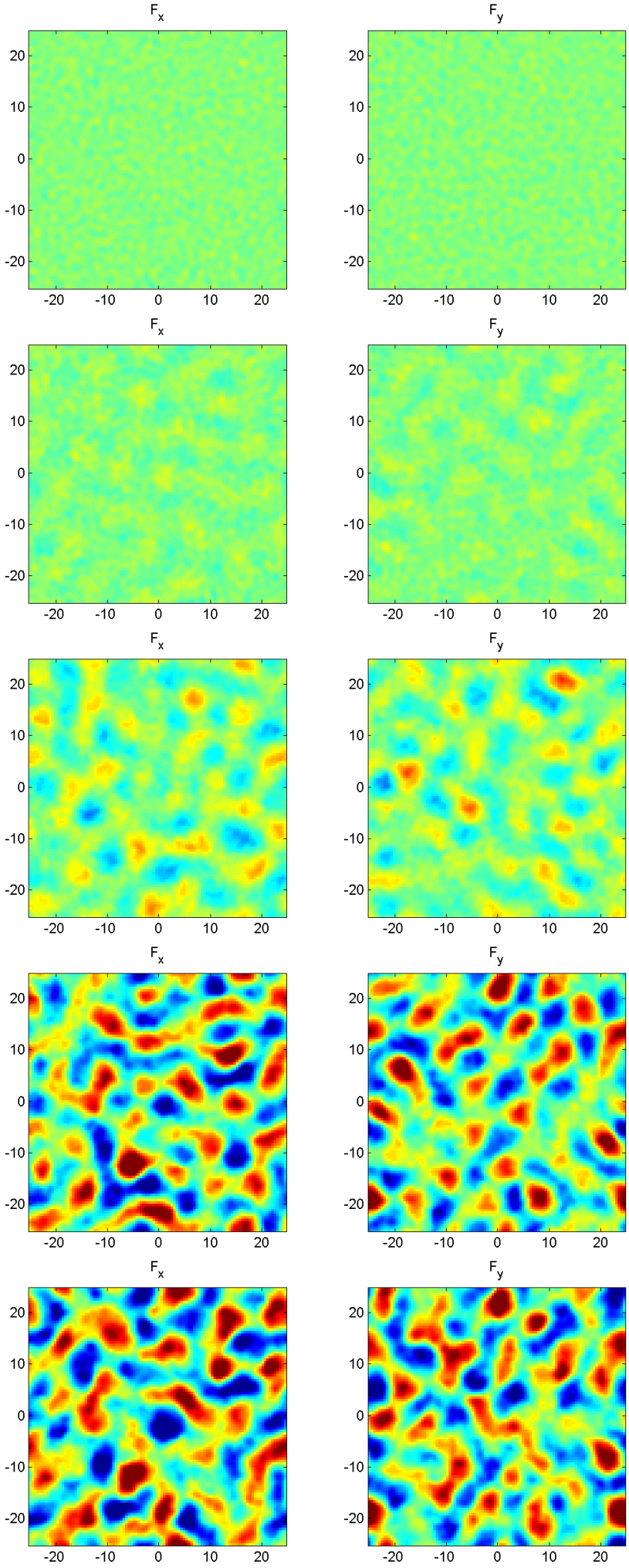

Figure 4.8: Spontaneous magnetization of a polar state, with experimental parameters as given in Sec. 3.4. Snapshots taken at times given by Fig. 4.6; i.e., $t = 0$, 3, 5, 7, and 9ms.

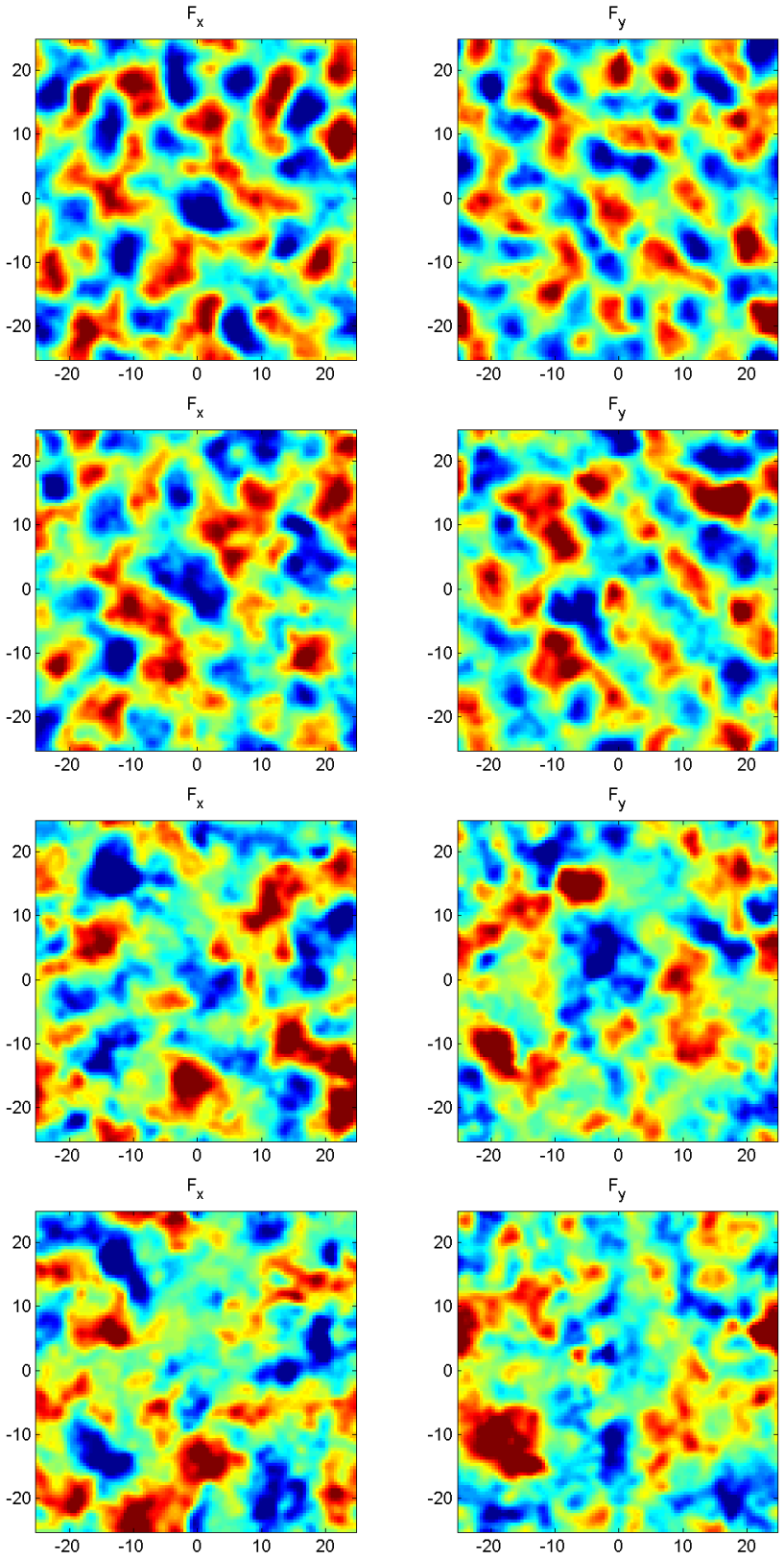

Figure 4.9: Observation of 'coarsening' in long-time dynamics. Here the condensate reaches the prethermalized regime, where domains grow and evolve randomly with no clear characteristic domain width. Parameters and axes as in the previous figure; snapshots taken at 11, 14, 22, and 29ms.

4.3 Quench Dynamics

Here's where the fun starts. Barnett *et al.* only reported quenches to $q = 0$. In this section we investigate the effect of *different quench depths* — i.e., the different final quadratic Zeeman parameters in the range $q = 0 \rightarrow 2|g_s|n$, where the initial polar phase is unstable (c.f. Fig. 2.6). We look at the effect on domain formation – the average size of the formed domains, how long it takes to form, and how strongly magnetized they are.

Recall from Sec. 2.3.3 when we introduced correlation functions. Here we construct the spatial correlation function for our condensate at each iteration of our code and from it define an average domain size for the condensate. Equation 2.40 gives us an average of how strongly correlated any point in our condensate is to any other point distance $\mathbf{r}$ away, and hence a way to explicitly define an average domain size for the condensate. It also allows us to look at how ordered the magnetization of our condensate is at any point in time.

We start with an initial polar state with vacuum noise:

$$\Psi = \begin{bmatrix} \psi_+ \\ \psi_0 \\ \psi_- \end{bmatrix}$$

where

$$\psi_i(\mathbf{r}) = \sqrt{n}\delta_{i0} + \frac{\mathcal{R}_{Re} + i\mathcal{R}_{Im}}{2l} \quad i = +1, 0, -1 \tag{4.7}$$

Here, $\mathcal{R}$ are random numbers of order unity obeying a Gaussian distribution of mean zero and variance 1. Plotting this, we see it's reminiscent of a 2D sinc function with background noise:

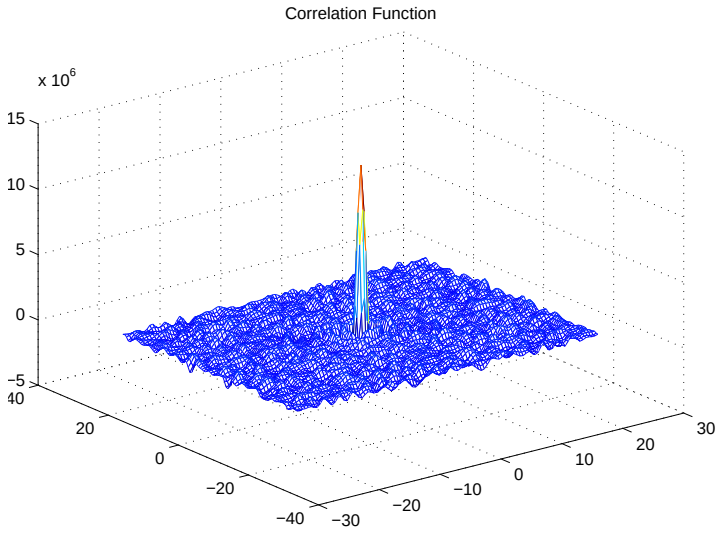

Figure 4.10: The 2D correlation function for the initial state, where the axes represent x and y separation.

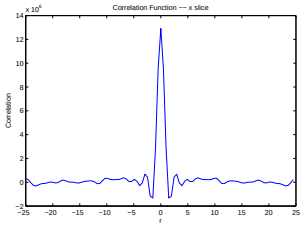

Figure 4.11: A slice through the correlation function taken at $x = 73$, the midpoint of the grid. Note the sinc-like behaviour.

Because the correlation function displays behaviour much like the sinc function (as seen in Fig. 4.11), we will define the average domain size to be the width of the main peak of the function at $\mathbf{r} = 0$. We take measurements through both the x and y planes and average them out to find the average domain size of the condensate at that time.

It is important to note here that domain size and the magnetization of the domains do not always correspond to each other. Hence we also keep

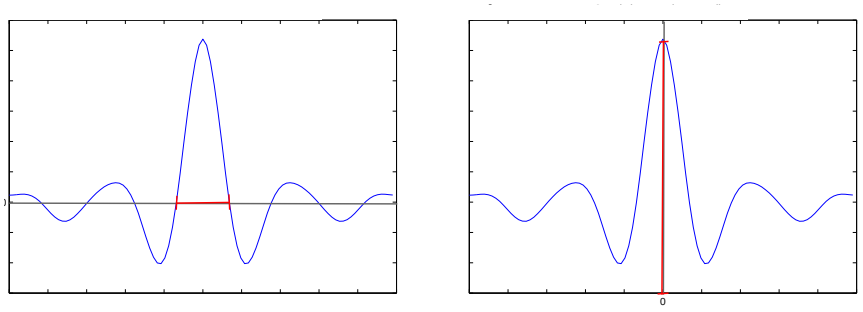

Figure 4.12: Schematic diagram of how the width and peak is measured in our quenching studies. The width is measured from the center out to the first zero crossing in both directions. We repeat this for a slice in the y axis, and average the two out. Peak value is measured to be the correlation value at $r = 0$, and the mean is simply the sum of all values of the correlation function, averaged over all grid points.

track of correlation strength — i.e., a measure of how magnetized these domains are. We do this by taking the peak and mean value of the 2D correlation function.

We should remind ourselves what these values actually mean, and remember that we've removed all spatial dependence in them. The peak correlation, taken at $G(0)$, is a measure of how strongly magnetized each individual grid point is, while the mean correlation tells us how magnetized the *entire condensate* is.

As usual, it is good practice to always keep an eye on our condensate fraction, albeit merely for troubleshooting purposes.

4.3.1 Sampling Pass

Despite extensive investigation into the short and long time dynamics of a quench to $q_f = 0$, Barnett *et al.* did not look at any quenches to $q_f \neq 0$. This is actually quite a curious region, if one will recall from Sec. 2.3.3: previous theoretical work by Lamacraft detailed different quenching regimes within $0 < q_f < 2|g_s|n$.

To get a broad overview of what the quench dynamics look like at different quadratic Zeeman, we perform a sampling pass of five equally spaced points between $q_f = 0$ and $q_f = 2|g_s|n$ (see Fig. **??**)

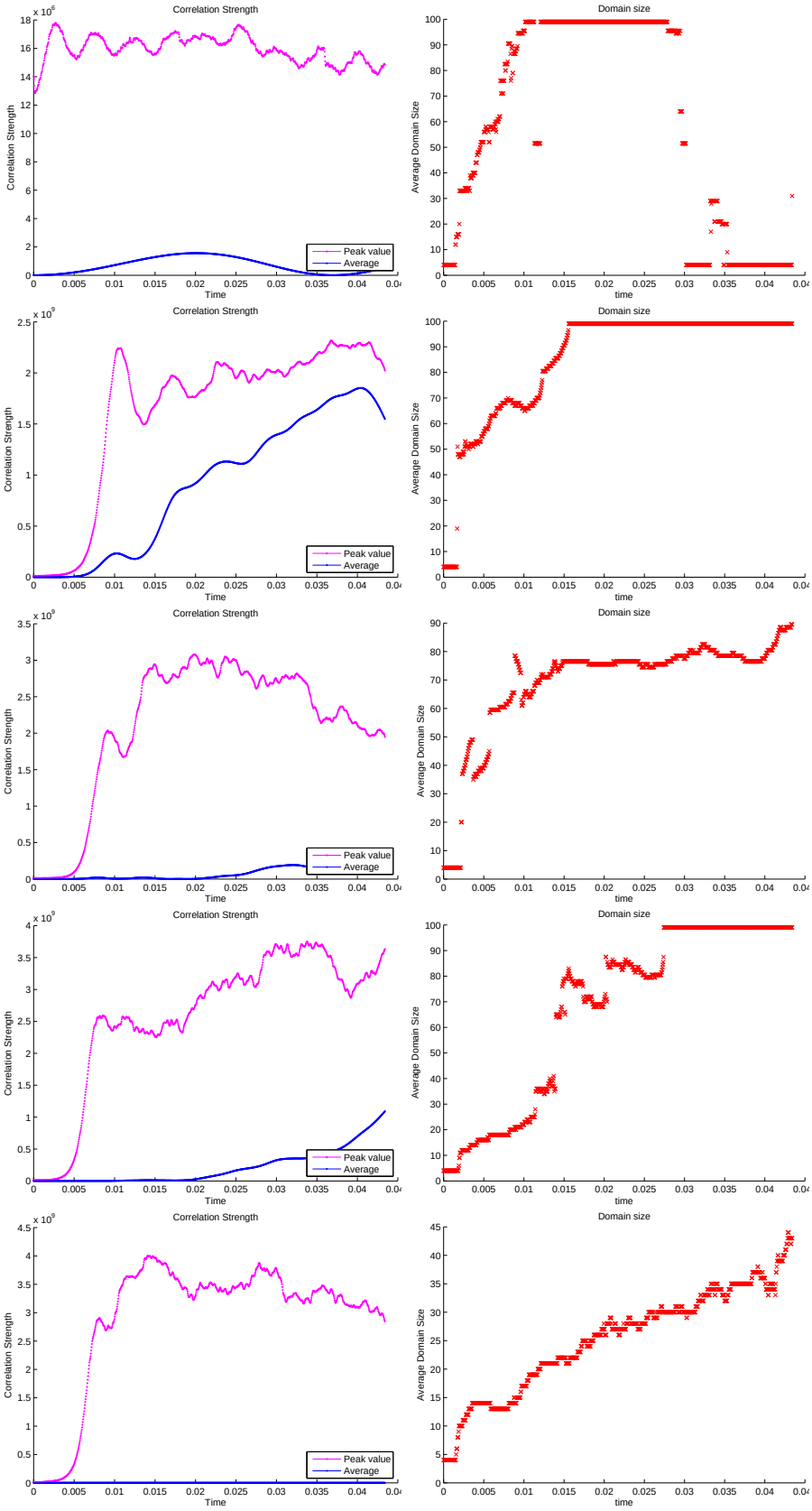

Figure 4.13: A sample run of five simulations quenching to q_f values of 2, 1.5, 1, 0.5, and 0, respectively from top to bottom. For $q_f = 0$, the correlation function shows expected dynamics (c.f. Fig. 4.6). One should also recall that in the previous section, we found that long-time, random coarsening dynamics started somewhere around $\sim 10ms$, which explains the continued growth of domain size after it first it levels out for $q_f = 0$.

From data gathered in our sampling pass, we make three remarks:

1. Clipping in domain size. The right hand column of Fig. 4.13 shows the average domain width in the condensate as defined previously. However, this tends to 'clip' (i.e., max out) when the width reaches, or surpasses, the entire length of the condensate. This happens when our system tends to the same spin state and becomes, in general, more correlated. The entire correlation function lifts above zero, and hence our domain width becomes undefined. We can observe this in Fig. 4.13 principally when the mean value of the correlation function rises above zero, meaning that the value of overall transverse magnetization deviates.

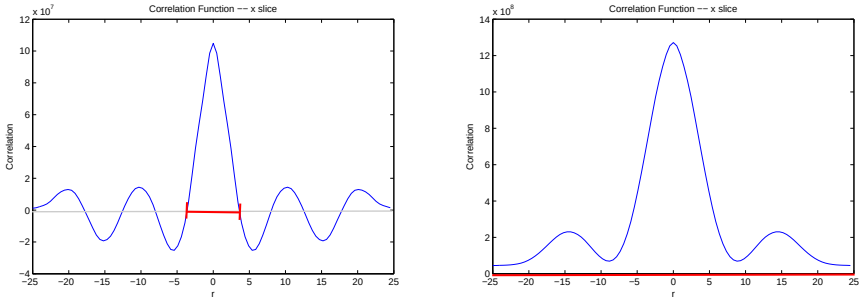

Figure 4.14: Lifting of the correlation functions over time. When the condensate first starts forming domains, its correlation function looks qualitatively akin to the sinc-like function on the left. Afterwards, the entire correlation function is 'lifted' up above zero (note the y-axis limits on the right subfigure).

2. Coarsening. Throughout this investigation we've talked about 'coarsening', and have roughly defined it to mean randomly growing spin textures with no characteristic length (i.e., it is *fractal* in nature). During this long-time regime, the chaotic behavior of the system renders each simulation run-dependent[1], and any thorough data analysis will involve statistics collected from many repeated simulations. Hence we will look at the long-time regime only qualitatively. Thankfully, the phenomenon of coarsening shows itself quite distinctively and reliably in the correlation view:

[1] We know this is the case as each q_f has been run at least three to five times. However, simulations display qualitatively similar properties for similar q_f.

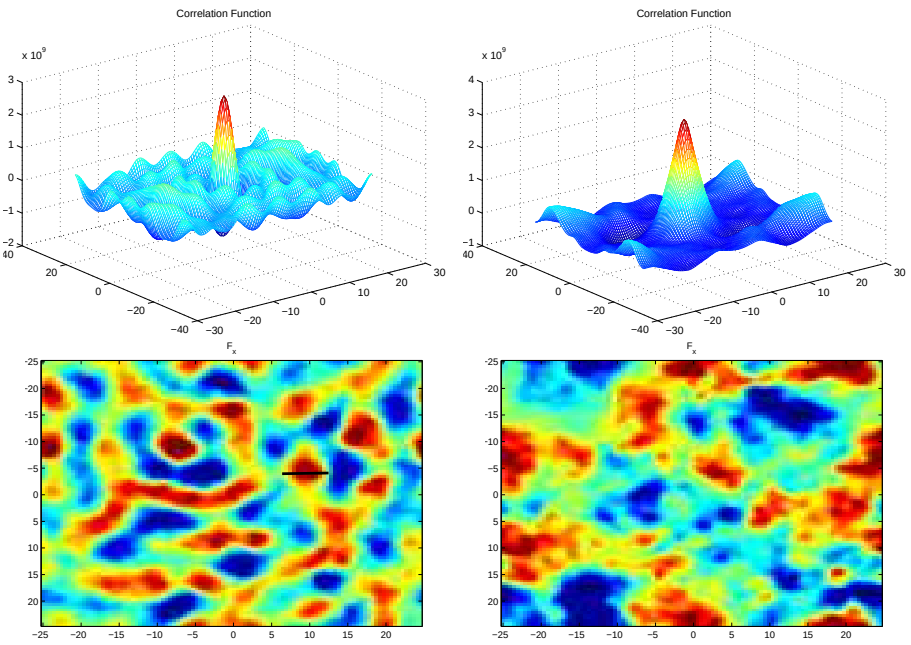

Figure 4.15: Snapshots during a quench to $q_f = 0$ of (left) well-formed domains in the short-time regime, and (right) coarsening effects. The black line on the bottom left denotes how our definition of average domain size from the correlation function translates to F_+.

During the initial domain-formation phase after the quench, domains are well-defined and all have similar sizes. Its correlation function at this point resembles a smooth, 2D sinc function. When we define the average width of the domains to be the distance from the original at which the

correlation function crosses zero, this translates to the midpoint between the two directions the spinors could be pointing to in the transverse plane — i.e., the unpolarized spinors, denoted by the greens (and more explicity by the black line) in Fig. 4.15.

Going into long-time dynamics, the edges of the correlation function start flattening out, and the base of the central peak widens. In the prethermalized, coarse regime, the correlation function displays a cone shape, signifying domains in a range of sizes. Take note that this was qualitatively the exact same behavior as observed by Barnett *et al.*

3. Peak and mean behavior. Though clearly related, the peak and mean values of our correlation function displays somewhat disparate behavior (see Fig. 4.13). The peak value stays small at shallow quenches, eventually getting larger and more ordered at deeper quenches. Peak correlation values also tend to flatten out and displays less oscillatory behavior at deeper quenches (this is what we expect to see – c.f. Fig. 2.16). The mean value, however, lifts above zero *between* $q_f = 0$ and $q_f = 2|g_s|n$.

Curious. We may have set sail looking for quench depth effects on domain size, but we happened upon a funny new island. This just begs for further investigation, so we'll consider this more in-depth in the next section.

4.3.2 Effect of Varied Quench Depth

Doing one better than our initial sample pass, we run our simulations for twenty equally spaced quench depths between $q_f = 0$ and $q_f = 2|g_s|n$. Each run is propagated for $\sim$ 25ms (6000 iterations), at least[2].

[2] Note that a single run at a specified quench depth takes just over an hour to finish; hence five runs of the same simulation will take 5-6 hours. Patience is key!

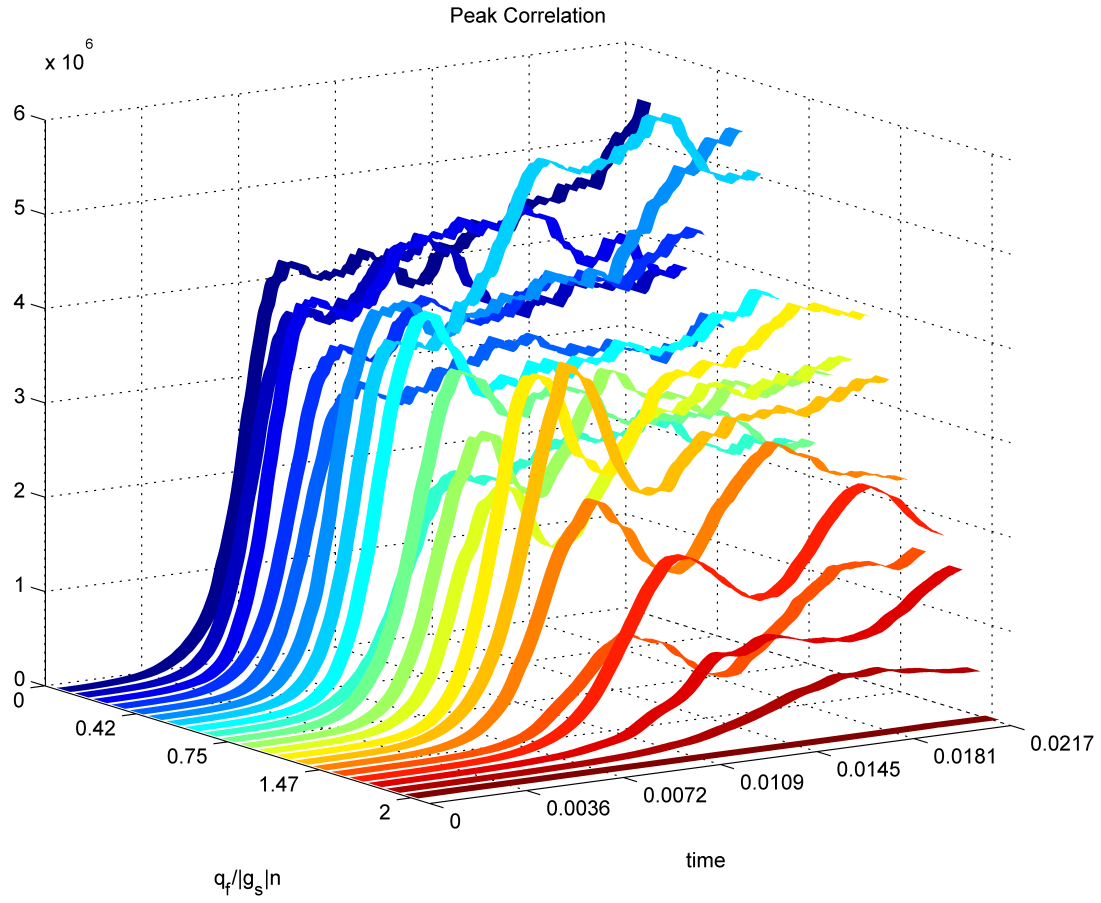

Figure 4.16: Peak values for the 2D correlation function at varied quench depths in time.

On the peak correlation value

Fig. 4.16 shows good agreement with previous quenching studies by Barnett *et al.* in the deep quench limit ($q_f = 0$). We see an exponential rise in magnetized domains, which then plateaus out to a quasi-steady, prethermalized regime. This happens similarly for the other deep quenches ($q_f < 1|g_s|n$), with lessening degrees of magnetization as we move to shallower quenches. This makes sense due to the fact that we're putting less energy into the system at shallower quench depths.

We can look into this excess energy further, by looking at the heating of the system, given by Barnett *et al.*:

$$Q = \frac{1}{4} N q_0 (1 - \frac{q_f}{q_0})^2 \tag{4.8}$$

Plotting this:

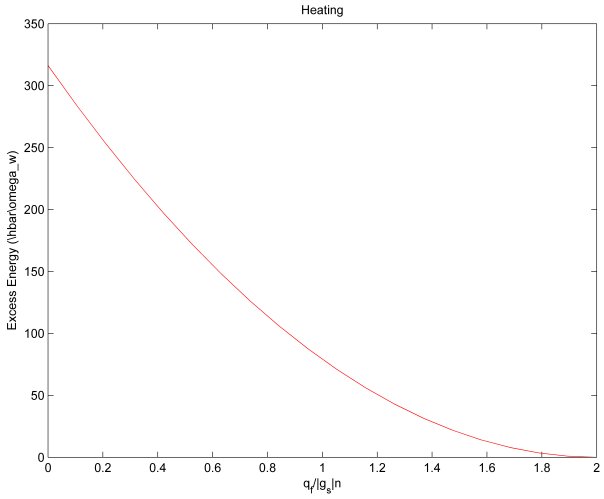

Figure 4.17: Excess energy after a quench.

And we observe that a deeper quench results in us putting more excess energy into the system. This excess energy corresponds nicely with the curves in Fig. 4.16.

What is interesting and must be discussed is the lesser-studied regime of shallow quenches ($1|g_s|n < q_f < 2|g_s|n$), shown by the yellows, oranges and reds in Fig. 4.16. Here we see almost well-defined oscillations, characteristic of correlations propagated along a *light-cone*. When we say this, we mean that the propagation of correlations has a *finite* velocity, $c_s = -(q(q - 2|g_s|n))/k_c^2$. This gives a similar situation as in general relativity, where information has a finite and constant speed limit. The oscillatory behavior of correlations displayed in the shallow quench regime is reminiscent of similar investigations performed on light-cone dynamics in quantum many-body systems (see, for example, Fig. 2 in Ref.[41], which performs a quench in an optical lattice).

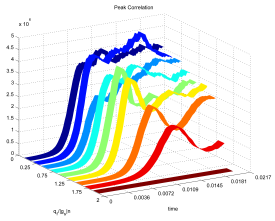

Figure 4.18: Peak correlation values for 5 equally spaced runs between $q_f = 0$ and $q_f = 2|g_s|n$.

We were surprised by the regularity of these oscillations, but did not have time to perform a more thorough, focused investigation in this area.

Here the reader may inquire into some fluctuations between the results shown here. We want to stress that our system has many degrees of freedom (simulating the interaction of tens of thousands of modes) and subject to chaotic behavior. Though single runs of each simulation may display distinct behavior, the overall tend is reasonably clear.

Ideally, with more time and computational resources, an extension would be to run this set of simulations for many times, and average out the results over many trajectories. With this we could also assess the typical amount of fluctuation from the mean.

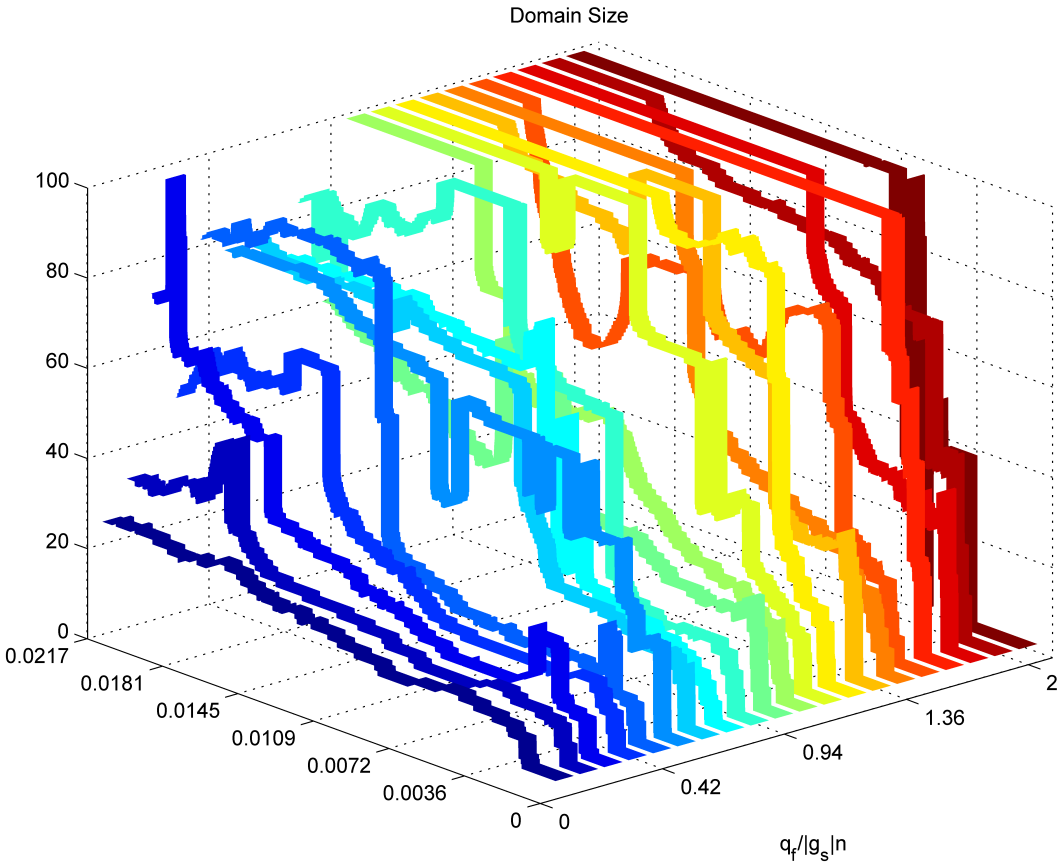

Figure 4.19: Average domain sizes in the condensate at varied quench depths in time. Note the jagged character of these plots come from our initial definition of domain width. During the simulation, the entire correlation tends to lift for quenches $0 < q_f < 2|g_s|n$. When this happens, the first minimum of the sinc function rises above zero, and our calculation jumps to the next zero-crossing.

On the average domain size

A look at the evolution of domain sizes in our system yields a very different picture. Here, it is the shallow quenches near $q_0 = 2|g_s|n$ that spawn the largest domain sizes (albeit mostly uncorrelated), while the deep quenches take on more modest domain sizes (and are highly ordered).

For deeper quenches we add more excess energy to the system; hence, shorter wavelength modes can become unstable, leading to smaller domain sizes, and respectively for shallow quenches: only long wavelengths become unstable; hence the larger domain sizes.

From the domain size, and peak correlation data, we can conclude that we have a 'can't have your cake and eat it too' situation. If we want stronger correlations (more order) we have to sacrifice homogeneity by introducing more domain walls (more entropy). If we want a very smooth-looking condensate, we can't have them be highly correlated to each other.

Looking at the relationship between quench depth and domain size is not so trivial. Due to the inevitability of coarsening effects that break and grow our initially nice domains, we take all measurements of domain size during the short-time regime – at 1680 iterations, or around 6ms. The zero-crossing method of finding our domain sizes also has limitations: prior to starting these simulations we did not suspect that the entire correlation function would lift (most dramatically around $q_f \approx 1|g_s|n$). This meant

that sometimes the first minimum of our sinc function rises above zero, and the algorithm would sample the second, third minima, or even just the bounds of the grid, as the domain width. Hence the reason for the strange discrete jumps one sees in Fig. 4.19.

Despite these jumps, we can still clearly see an overall growth in domain sizes as we go from $q_f = 0$ to shallower quenches:

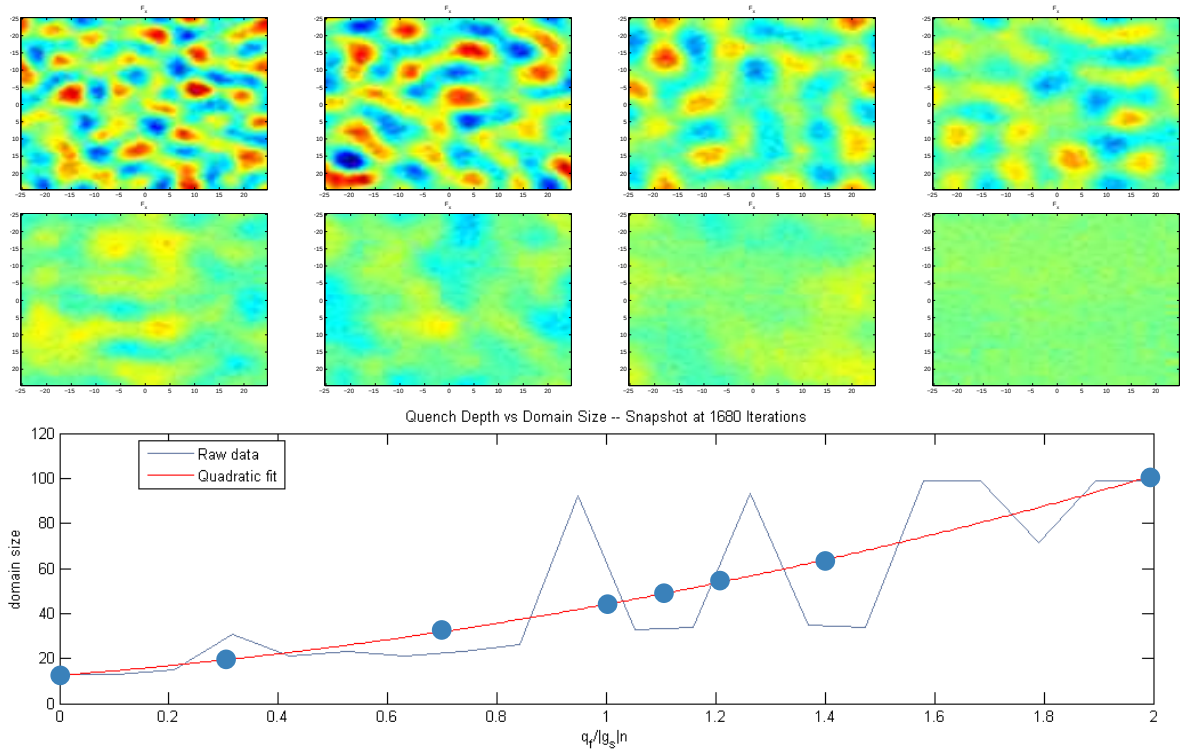

Figure 4.20: Snapshots of transverse magnetization of our condensate for various quench depths (denoted by the blue dots).

This lifting of the entire correlation function was somewhat problematic and definitely unexpected. Future work would benefit from better statistics (i.e. more trajectories for each quench depth), and a different procedure to find the domain widths. A common way to do this is to find the first two minima of the correlation function, going out from the center.

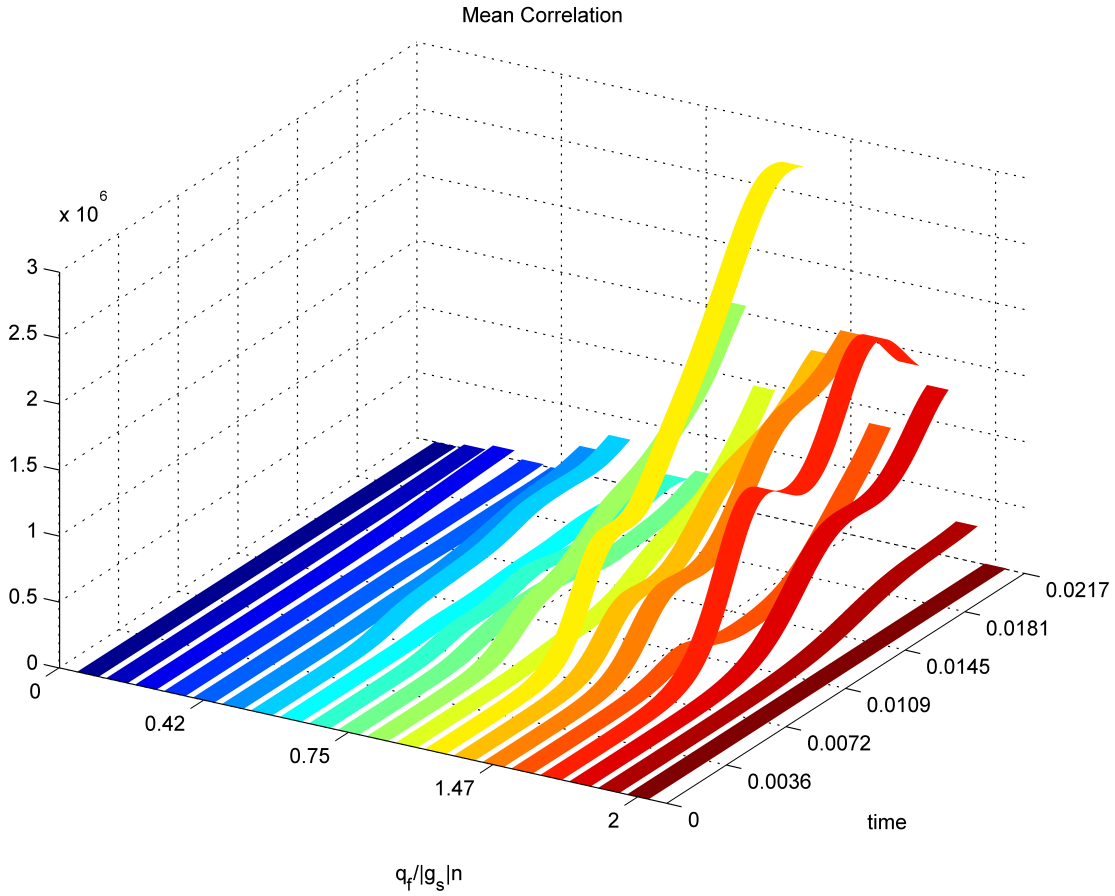

Figure 4.21: Mean correlation values for varied quench depths in time.

On the mean correlation value

Between the quench depths of $q_f = 0$ and $q_f = 2|g_s|n$, the mean value of the correlation function — expected to stay at zero — lifts, peaking for values of $q \approx 1|g_s|n$. This also appears to be more prominent for shallow quenches, as seen in Fig. 4.21, with some cases rising six orders of magnitude above their original values. For some reason or another, the *entire condensate* becomes more spatially correlated; more ordered.

What is actually happening when the mean correlation rises? We take a look to the transverse magnetization and actual correlation function during these times to find out. Fig. 4.22 shows what this 'lifting' corresponds to: the averaged overall transverse magnetization $\overline{F_+}$ becomes nonzero, and the condensate enters a phase of added correlation; it becomes globally ordered.

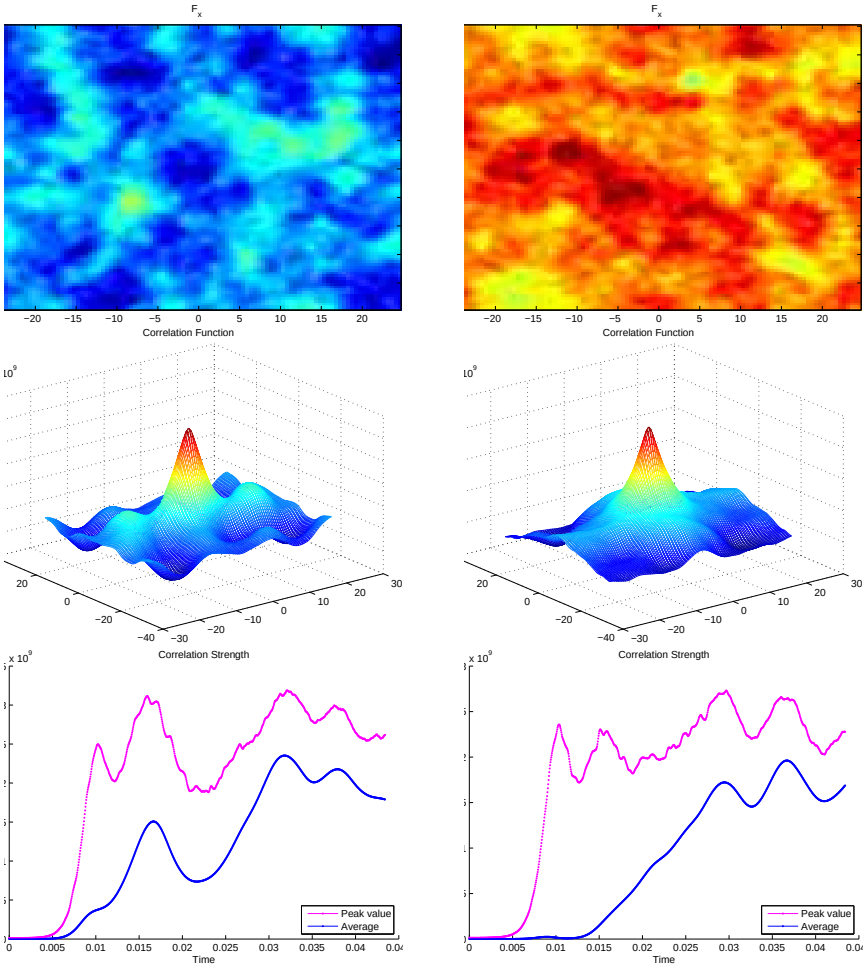

Figure 4.22: Transverse magnetization of a quench to $q_f = 1.2|g_s|n$ (left) and $q_f = 1.3|g_s|n$ (right) at $\sim$ 45ms, and their corresponding correlation functions, and time evolution. Notice how the condensate is highly magnetized (i.e., on either end of the color spectrum) in general.

This is somewhat peculiar, as one may recall from Sec. 2.3.2, spin oscillations reached a "spin-mixing resonance" at exactly $q = 1|g_s|n$! Could these two phenomena be linked in some way? We also suspect, due to this ordering being more prevalent in the shallow quench regime, that this may result from the light-cone propagation properties of the correlations in that regime.

Regardless, this peculiarity is definitely a place for further study in the future.

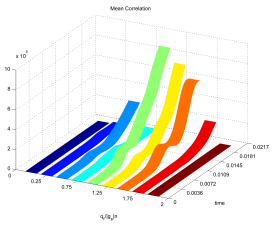

Figure 4.23: Initial plot of mean correlation values for 5 equally spaced quenched depths. Note the maximum at $q_f = 1|g_s|n$.

Chapter 5

Conclusion

It has been shown in this dissertation that quenches at differing depths holds plenty of rich, unexplored dynamics; especially that of the shallow-quench regime.

In this thesis we developed code from scratch to successfully simulate a complex, multi-modal spinor Bose-Einstein condensate using the fourth and fifth order Runge-Kutta-Fehlberg algorithm, modified for a spinor system with vector order parameter. Our code was subjected to endless testing and modifying, reaching the needed efficiency and accuracy needed to simulate a spinor system. We replicated known properties such as coherent spin-mixing oscillations, and reproduced prethermalization results from Barnett *et al.*'s quench to $q = 0$.

With this under our belt, we set forth to investigate dynamics at different quench depths in the broken-axis phase between $q = 0$ and $q = 2|g_s|n$. This was extremely computationally expensive, and required runs at twenty different quench points, propagating out until long-time dynamics and coarsening were observed. This payment was not without reward, however — our results show a multitude of interesting things.

First, we learned how the system orders itself at different depths. Shallow quenches lead to large spatial coherence, though that coherence remains almost negligible. Deep quenches saw the formation of small, highly correlated (i.e., magnetized) domains.

During this, we also characterized the phenomenon of 'coarsening' through our correlation function, and observed our condensate reach a prethermalized regime, *à la* Barnett *et al.*

Curiously, we observed a 'lifting' of the mean value of the correlation function. This peaked near $q_f \approx |g_s|n$, and waned to zero before $q_f = 0$ and $q_f = 2|g_s|n$. This was particularly peculiar, as it physically translates into a gradual rise of *order* — i.e., the system becomes more magnetized overall. We have many suspicions about what could be causing such dynamics here — this is definitely a place to do more research in the future.

5.1 Future Prospects

We must stress again that this is a large, complex, multi-nodal system which is mostly unexplored. Hence, the opportunity for future work is vast.

First, a natural follow up to the research presented in this dissertation is to simply run the same simulations again, and for many times. Due to the chaotic nature of our system, each run displays distinct behavior. It would be helpful to have been able to obtain an average of many trajectories (and how much they fluctuated).

Secondly, we already saw some interesting dynamics inside the shallow-quench regime. This is a good place to begin study towards the light-cone behavior of correlation propagation, thus leading us to investigations in quantum information theory and relativistic quantum mechanics — a very exciting journey indeed.

And finally, an investigation into the gradual, but spontaneous ordering of the entire condensate around $q_f = |g_s|n$.

References

[1] W. Zurek, "Cosmological experiments in superfluid helium?," *Nature*, vol. 317, no. 6037, pp. 505–508, 1985.

[2] T. W. Kibble, "Topology of cosmic domains and strings," *Journal of Physics A: Mathematical and General*, vol. 9, no. 8, p. 1387, 1976.

[3] S. Bose, "Plancks law and the light quantum hypothesis," *Journal of Astrophysics and Astronomy*, vol. 15, no. 1, pp. 3–7, 1994.

[4] M. H. Anderson, J. R. Ensher, M. R. Matthews, C. E. Wieman, and E. A. Cornell, "Observation of bose-einstein condensation in a dilute atomic vapor," *Science*, vol. 269, no. 5221, pp. 198–201, 1995.

[5] S. Inouye, M. Andrews, J. Stenger, H.-J. Miesner, D. Stamper-Kurn, and W. Ketterle, "Observation of feshbach resonances in a bose–einstein condensate," *Nature*, vol. 392, no. 6672, pp. 151–154, 1998.

[6] H.-J. Miesner, D. M. Stamper-Kurn, J. Stenger, S. Inouye, A. P. Chikkatur, and W. Ketterle, "Observation of metastable states in spinor bose-einstein condensates," *Phys. Rev. Lett.*, vol. 82, pp. 2228–2231, Mar 1999.

[7] A. Lamacraft, "Quantum quenches in a spinor condensate," *Physical review letters*, vol. 98, no. 16, p. 160404, 2007.

[8] R. Barnett, A. Polkovnikov, and M. Vengalattore, "Prethermalization in quenched spinor condensates," *Phys. Rev. A*, vol. 84, p. 023606, Aug 2011.

[9] L. Mathey and A. Polkovnikov, "Light cone dynamics and reverse kibble-zurek mechanism in two-dimensional superfluids following a quantum quench," *Physical Review A*, vol. 81, no. 3, p. 033605, 2010.

[10] D. M. Stamper-Kurn and M. Ueda, "Spinor bose gases: Symmetries, magnetism, and quantum dynamics," *Reviews of Modern Physics*, vol. 85, no. 3, p. 1191, 2013.

[11] Y. Kawaguchi, H. Saito, and M. Ueda, "Spontaneous circulation in ground-state spinor dipolar bose-einstein condensates," *Phys. Rev. Lett.*, vol. 97, p. 130404, Sep 2006.

[12] M. Vengalattore, J. Guzman, S. R. Leslie, F. Serwane, and D. M. Stamper-Kurn, "Periodic spin textures in a degenerate $f = 1$ ^{87}Rb spinor bose gas," *Phys. Rev. A*, vol. 81, p. 053612, May 2010.

[13] T.-L. Ho, "Spinor bose condensates in optical traps," *Phys. Rev. Lett.*, vol. 81, pp. 742–745, Jul 1998.

[14] Y. Kawaguchi and M. Ueda, "Spinor bose-einstein condensates," *Physics Reports*, 2012.

[15] J. Stenger, S. Inouye, D. Stamper-Kurn, H.-J. Miesner, A. Chikkatur, and W. Ketterle, "Spin domains in ground-state bose–einstein condensates," *Nature*, vol. 396, no. 6709, pp. 345–348, 1998.

[16] Y. Nambu, "Quasi-Particles and Gauge Invariance in the Theory of Superconductivity," *Physical Review*, vol. 117, pp. 648–663, 1960.

[17] J. Goldstone, "Field theories with superconductor solutions," *Il Nuovo Cimento*, vol. 19, no. 1, pp. 154–164, 1961.

[18] J. Goldstone, A. Salam, and S. Weinberg, "Broken symmetries," *Phys. Rev.*, vol. 127, pp. 965–970, Aug 1962.

[19] N. Bogoliubov, "On the theory of superfluidity," *J. phys.(UssR)*, vol. 11, no. 23, pp. 4–2, 1947.

[20] A. L. Fetter and J. D. Walecka, *Quantum theory of many-particle systems*. Courier Dover Publications, 2003.

[21] N. Parker, *Numerical Studies of Vortices and Dark Solitons in Atomic Bose-Einstein Condensates*. PhD thesis, University of Durham, October 2004.

[22] W. Zhang, D. L. Zhou, M.-S. Chang, M. S. Chapman, and L. You, "Coherent spin mixing dynamics in a spin-1 atomic condensate," *Phys. Rev. A*, vol. 72, p. 013602, Jul 2005.

[23] D. R. Romano and E. J. V. de Passos, "Population and phase dynamics of $f = 1$ spinor condensates in an external magnetic field," *Phys. Rev. A*, vol. 70, p. 043614, Oct 2004.

[24] M.-S. Chang, Q. Qin, W. Zhang, L. You, and M. S. Chapman, "Coherent spinor dynamics in a spin-1 bose condensate," *Nature Physics*, vol. 1, no. 2, pp. 111–116, 2005.

[25] J. Kronjäger, C. Becker, P. Navez, K. Bongs, and K. Sengstock, "Magnetically tuned spin dynamics resonance," *Phys. Rev. Lett.*, vol. 97, p. 110404, Sep 2006.

[26] A. T. Black, E. Gomez, L. D. Turner, S. Jung, and P. D. Lett, "Spinor dynamics in an antiferromagnetic spin-1 condensate," *Phys. Rev. Lett.*, vol. 99, p. 070403, Aug 2007.

[27] L. Sadler, J. Higbie, S. Leslie, M. Vengalattore, and D. Stamper-Kurn, "Spontaneous symmetry breaking in a quenched ferromagnetic spinor bose–einstein condensate," *Nature*, vol. 443, no. 7109, pp. 312–315, 2006.

[28] H. Pu, C. Law, S. Raghavan, J. Eberly, and N. Bigelow, "Spin-mixing dynamics of a spinor bose-einstein condensate," *Physical Review A*, vol. 60, no. 2, pp. 1463–1470, 1999.

[29] H. Saito, Y. Kawaguchi, and M. Ueda, "Topological defect formation in a quenched ferromagnetic bose-einstein condensates," *Physical Review A*, vol. 75, no. 1, p. 013621, 2007.

[30] E. J. Weinberg and A. Wu, "Understanding complex perturbative effective potentials," *Phys. Rev. D;(United States)*, vol. 36, no. 8, 1987.

[31] A. Polkovnikov, K. Sengupta, A. Silva, and M. Vengalattore, "*Colloquium* : Nonequilibrium dynamics of closed interacting quantum systems," *Rev. Mod. Phys.*, vol. 83, pp. 863–883, Aug 2011.

[32] P. Blakie, A. Bradley, M. Davis, R. Ballagh, and C. Gardiner, "Dynamics and statistical mechanics of ultra-cold bose gases using c-field techniques," *Advances in Physics*, vol. 57, no. 5, pp. 363–455, 2008.

[33] J. H. Mathews and K. K. Fink, *Numerical Methods Using Matlab (4th Edition)*. Prentice Hall, 4 ed., Jan. 2004.

[34] J. R. Cash and A. H. Karp, "A variable order runge-kutta method for initial value problems with rapidly varying right-hand sides," *ACM Trans. Math. Softw.*, vol. 16, pp. 201–222, Sept. 1990.

[35] W. Press, *Numerical Recipes 3rd Edition: The Art of Scientific Computing*. Cambridge University Press, 2007.

[36] A. Sinatra, C. Lobo, and Y. Castin, "The truncated wigner method for bose-condensed gases: limits of validity and applications," *Journal of Physics B: Atomic, Molecular and Optical Physics*, vol. 35, no. 17, p. 3599, 2002.

[37] J. Emsley, *The Elements*. Oxford Chemistry Guides, New York, NY: Oxford Univ. Press, 1995.

[38] M. Egorov, B. Opanchuk, P. Drummond, B. V. Hall, P. Hannaford, and A. I. Sidorov, "Measurement of s-wave scattering lengths in a two-component bose-einstein condensate," *Phys. Rev. A*, vol. 87, p. 053614, May 2013.

[39] S. R. Leslie, J. Guzman, M. Vengalattore, J. D. Sau, M. L. Cohen, and D. M. Stamper-Kurn, "Amplification of fluctuations in a spinor bose-einstein condensate," *Phys. Rev. A*, vol. 79, p. 043631, Apr 2009.

[40] D. Yan and T. Ma, "The gross-pitaevskii model of spinor bec," *Journal of Applied Mathematics*, vol. 2012, p. 14, 2012.

[41] M. Cheneau, P. Barmettler, D. Poletti, M. Endres, P. Schauß, T. Fukuhara, C. Gross, I. Bloch, C. Kollath, and S. Kuhr, "Light-cone-like spreading of correlations in a quantum many-body system," *Nature*, vol. 481, no. 7382, pp. 484–487, 2012.

[42] L. Pitaevskii and S. Stringari, *Bose-Einstein Condensation*. International Series of Monographs on Physics, Clarendon Press, 2003.